Cell

Article

Nuclear proteome reveals microtubule-associated protein regulating fate and disease

Graphical abstract

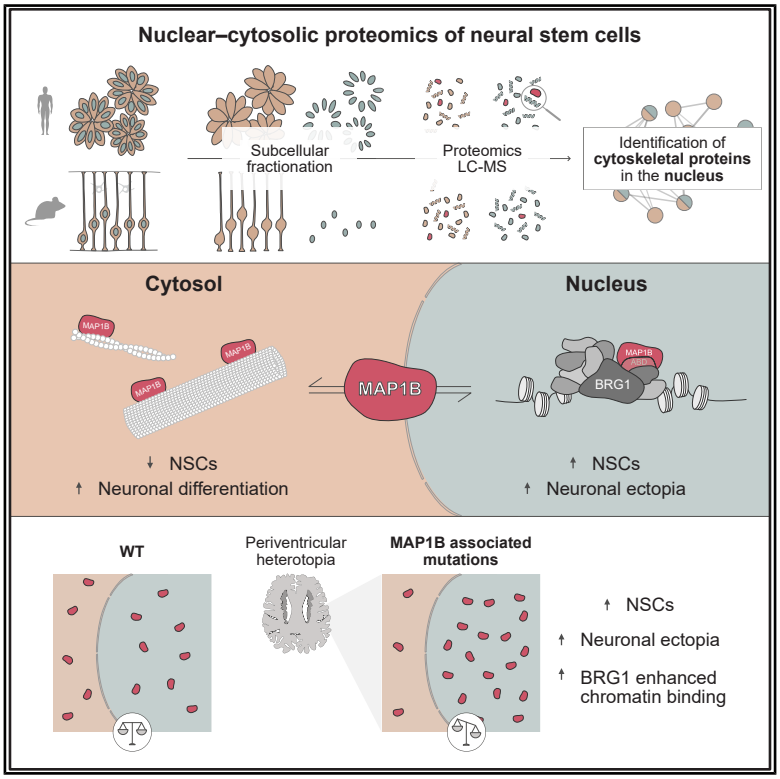

Highlights

- Nuclear and cytosolic proteomics reveal widespread nuclear cytoskeletal proteins
- MAP1B shuttles between compartments in NSCs and impacts differentiation
- MAP1B interacts with the BAF chromatin-remodeling complex in the nucleus
- Disease-linked mutated MAP1B shows nuclear enrichment and increased BRG1/BAF binding

Authors

Florencia Merino, Lucas Miranda, Aparajita Kumar, ..., Stefanie M. Hauck, Silvia Cappello, Magdalena Götz

Correspondence

magdalena.goetz@helmholtz-munich.de

In brief

Nuclear and cytoplasmic proteomics uncover a nuclear pool of cytoskeletal proteins, including MAP1B, whose shuttling to the nucleus increases BRG1/BAF chromatin association and regulates brain development.

Merino et al., 2026, Cell *189*, 1–18
August 6, 2026
https://doi.org/10.1016/j.cell.2026.05.019

CellPress

Please cite this article in press as: Merino et al., Nuclear proteome reveals microtubule-associated protein regulating fate and disease, Cell (2026), https://doi.org/10.1016/j.cell.2026.05.019

Cell

CellPress
OPEN ACCESS

Article

Nuclear proteome reveals microtubule-associated protein regulating fate and disease

Florencia Merino,[1,2,3] Lucas Miranda,[4] Aparajita Kumar,[1,2,3] Yiling Li,[1,2,3] Deepak Kumar Sundaramoorthy,[1,2] Juliane Merl-Pham,[5] Eva-Maria Schentarra,[6,7] Clemens Steinek,[6] Veronica Pravata,[1] Claire Kittock,[8,9] Martina Bürkle,[1,2] Bob A. Hersbach,[1,2,3] Javier Ferri Beneito,[1,2] Florian Giesert,[2] Ralf Jungmann,[6,7] Louis-Jan Pilaz,[8,9] Stefanie M. Hauck,[5] Silvia Cappello,[1,10,11] and Magdalena Götz[1,2,11,12,*]

[1]Medical Faculty, Division of Physiological Genomics, Biomedical Center, Ludwig-Maximilians-Universität, 82152 Planegg-Martinsried, Germany
[2]Institute of Stem Cell Research, Helmholtz Center Munich, 82152 Planegg-Martinsried, Germany
[3]Graduate School of Systemic Neuroscience, Ludwig-Maximilians-Universität, 82152 Planegg-Martinsried, Germany
[4]Research Group Statistical Genetics, Max Planck Institute of Psychiatry, 80804 Munich, Germany
[5]Metabolomics and Proteomics Core, Helmholtz Center Munich, 85764 Neuherberg, Germany
[6]Max Planck Institute of Biochemistry, 82152 Planegg-Martinsried, Germany
[7]Faculty of Physics, Center for Nanoscience, Ludwig-Maximilians-Universität, 81377 Munich, Germany
[8]Pediatrics and Rare Diseases Group, Sanford Research, Sioux Falls, SD 57104, USA
[9]Sanford School of Medicine, University of South Dakota, Sioux Falls, SD 57107, USA
[10]Max Planck Institute of Psychiatry, 80804 Munich, Germany
[11]SYNERGY, Excellence Cluster of Systems Neurology, Ludwig-Maximilians-Universität, 82152 Planegg-Martinsried, Germany
[12]Lead contact
*Correspondence: magdalena.goetz@helmholtz-munich.de
https://doi.org/10.1016/j.cell.2026.05.019

SUMMARY

Cellular differentiation and morphogenesis require the coordination between cytoskeletal remodeling and transcriptional programs, raising the question of how cytoskeletal information is conveyed to the nucleus. Here, we profile the nuclear and cytosolic proteome of human and murine neural stem cells (NSCs) and uncover abundant cytoskeletal proteins in the nucleus, including the microtubule-associated protein 1B (MAP1B), implicated in disease. We find that MAP1B shuttles to the nucleus where it interacts with the BRG1-containing chromatin remodeling complex. MAP1B's nuclear enrichment promotes NSC fate, as opposed to its cytosolic function promoting neuronal differentiation. *In vivo*, increasing the nuclear/cytosol ratio disrupts neuronal positioning, reminiscent of patients with MAP1B mutations. Mutant human brain organoids show aberrant MAP1B nuclear enrichment, enhanced BRG1 chromatin binding, and neuronal ectopia formation. Our study uncovers a nuclear pool of cytoskeleton-associated proteins, revealing their role in fate regulation during brain development and reshaping our understanding of neurodevelopmental disease etiology.

INTRODUCTION

Tissue development relies fundamentally on morphogenesis, regulated by the dynamic remodeling of the cytoskeleton as well as transcriptional programs driving cell fate and subtype specification. In this context, proteins linking cytoskeletal remodeling and transcription are of particular interest, such as the serum response factor (SRF) and the Yes-associated protein (YAP) pathways with critical roles in development.[1–4] Beyond these canonical pathways, a growing number of proteins have been found to link these compartments,[5,6] as revealed, for example, by organelle profiling. For instance, many nuclear proteins, such as splicing factors, have been identified at the centrosome, exerting important and distinct roles in both compartments.[7–9] Conversely, core components of the cytoskeleton such as β-actin (ACTB), tubulins, and intermediate filament proteins have also been detected in the nucleus.[10–14] However, there is no comprehensive analysis of the nuclear proteome in most cells, including neural stem cells (NSCs). While the role of nuclear ACTB has been studied,[15–19] a comprehensive view of other cytoskeleton-associated proteins in the nucleus and their function there remains largely unexplored. This is particularly relevant in development, when processes of morphogenesis and fate transition proceed in a coordinated manner.[20,21]

The relevance of studying cytoskeletal proteins in the nucleus is further justified by human disease. Mutations in cytoskeletal proteins are associated with several neurodevelopmental

Please cite this article in press as: Merino et al., Nuclear proteome reveals microtubule-associated protein regulating fate and disease, Cell (2026), https://doi.org/10.1016/j.cell.2026.05.019

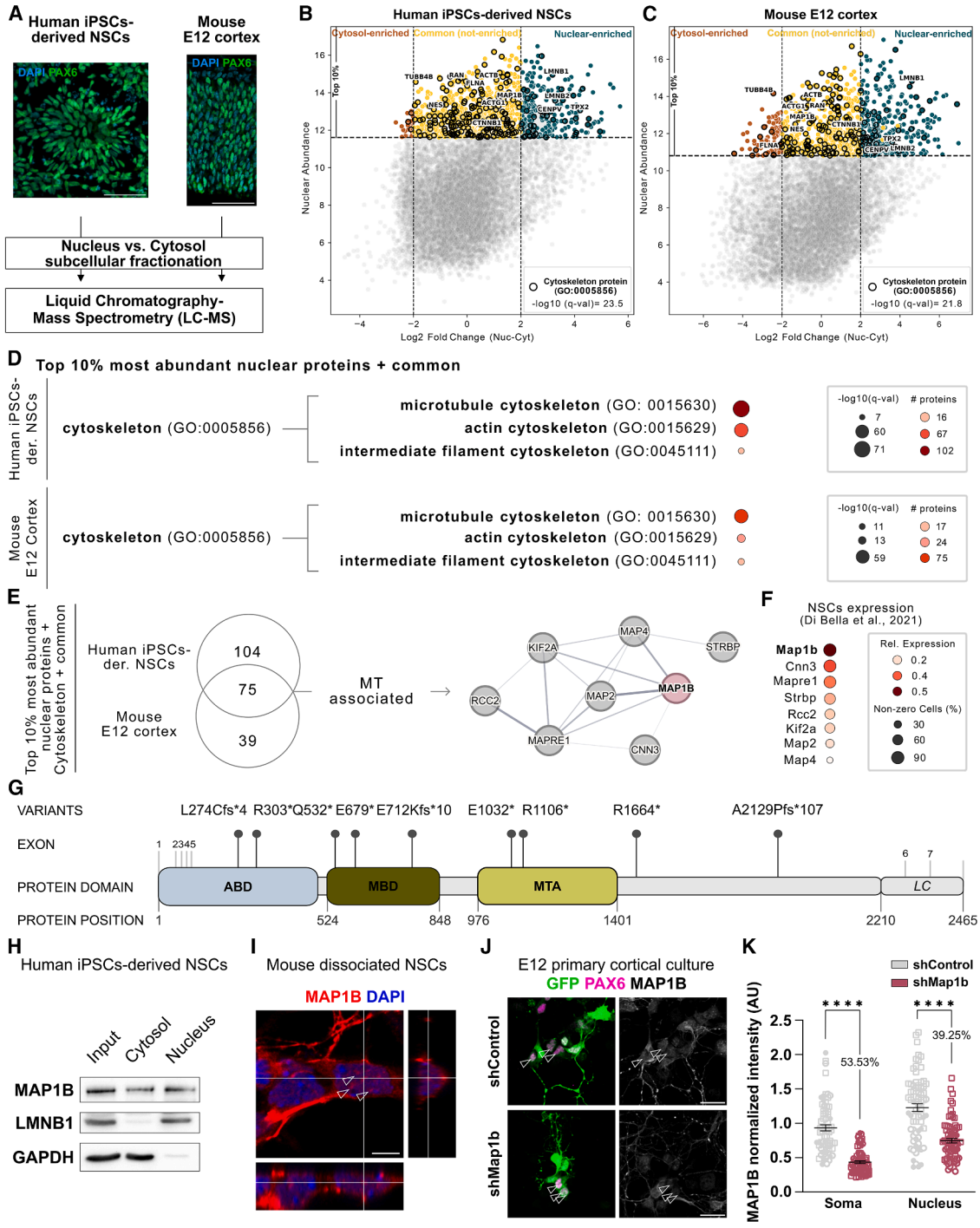

Figure 1. Cytoskeletal proteins are abundant in NSC nuclei

(A) Experimental design for profiling cytosolic and nuclear proteins in NSCs.

(B and C) Most abundant (10%) nuclear proteins within human iPSC-derived NSCs (B) and mouse E12 cortex (C) categorized based on cytosol vs. nuclear enrichment; colored dots correspond to cytosol-enriched (orange), common (yellow), or nuclear-enriched (blue) proteins. Highlighted proteins correspond to the GO term indicated.

(D) Dot plot representation of GO term analysis within the top 10% most abundant nuclear proteins, classified as "common" between the cytosol and nucleus, belonging to the GO term cytoskeleton (GO:0005856).

(E) Schematic overview of analysis. In the string network, the line thickness indicates the strength of the interaction.

(legend continued on next page)

Please cite this article in press as: Merino et al., Nuclear proteome reveals microtubule-associated protein regulating fate and disease, Cell (2026), https://doi.org/10.1016/j.cell.2026.05.019

diseases,[22] such as periventricular heterotopia (PH), where cells are found in ectopic positions at the lateral ventricles of the brain.[23,24] While classified as a neuronal migration disorder,[25] accumulating evidence shows that the proteins mutated in patients with this disease already have functions in NSCs.[7,26–28] Thus, unrecognized roles of disease-linked cytoskeletal proteins beyond regulating cell migration could help with understanding the mechanisms behind these disorders.

In this study, we profiled the cytoplasmic and nuclear compartments of murine and human NSCs, revealing a nuclear pool of several classes of cytoskeletal proteins. As a proof of principle, we focused on the microtubule (MT)-associated protein 1B (MAP1B), which we show shuttling between these compartments and regulating NSC maintenance vs. differentiation in an opposing manner. We found that MAP1B nuclear/cytoplasmic distribution is critical for brain development, as shown by the enriched nuclear localization of MAP1B with mutations from patients with PH. Our findings demonstrate that the subcellular distribution of cytoskeletal proteins directly controls NSC fate and brain development.

RESULTS

Cytoskeleton-associated proteins are abundant in the nuclei of human and murine NSCs

To gain a comprehensive view on nuclear proteins in NSCs, we performed nuclear-cytosolic fractionation of NSCs derived from human induced pluripotent stem cells (iPSCs) and murine embryonic day (E) 12 cerebral cortices, which are predominantly composed of NSCs,[29] followed by liquid chromatography-mass spectrometry (LC-MS) (Figure 1A). Over 10,000 and 9,000 proteins were identified in the human and murine samples, respectively (Table S1). Principal-component analysis (PCA) and Gene Ontology (GO) term analysis of proteins significantly enriched in either the cytosolic or nuclear fractions ($|\log_2$ fold change$| > 2$, $q < 0.05$), along with western blot (WB) analysis, confirmed effective subcellular separation (Figure S1; Table S1).

Focusing on the 10% most abundant nuclear proteins (Figures S2A and S2B), we detected well-known nuclear regulators of NSC identity, including the transcription factors and chromatin remodelers PAX6, GATAD2B, and SMARCA4 (BRG1, the ATPase of the SWI/SNF chromatin remodeling complex), as well as canonical nuclear proteins such as histones (H2AX, H4C1) and DNA-modifying enzymes (TOP2B, DNMT1, DNMT3A) in both human and mouse NSCs (Figures S2A and S2B). GO term analysis further supported our approach, with "nucleoplasm" (GO:0005654) as the most significant GO term for cellular compartments in both species and an overrepresentation of terms such as "stem cell differentiation" (GO:0048863) and "nervous system development" (GO:0007399) (Table S1). Most striking was the significant presence of proteins typically associated with other subcellular compartments (Table S1). These included high and consistent overrepresentation of cytoskeleton-associated proteins in the nuclei of both human and murine NSCs (Figures 1B and 1C; Table S1), highlighting the presence of a nuclear pool of all classes of cytoskeletal proteins.

Cytoskeletal proteins abundant in the nucleus were particularly prominent among proteins shared between nuclear and cytosolic fractions ($|\log_2$ fold change$| < 2$ and $q < 0.05$, defined as "common" proteins; Figures 1B and 1C), making cytosolic contamination an unlikely explanation, as such proteins would otherwise be more abundant in the cytosolic fraction. Instead, their dual localization could indicate active shuttling between the cytosol and nucleus. Indeed, among these, we identified well-known cytoskeleton-associated proteins known to shuttle between these compartments, such as ACTB,[30] β-catenin (CTNNB1),[31] and GTP-binding nuclear protein RAN,[32] involved in nucleocytoplasmic transport (Figures 1B and 1C; Table S1). Thus, this group of proteins may serve as potential linkers between cytoskeletal dynamics and the regulation of cell fate decisions and was therefore prioritized for validations and subsequent analysis (Figures S2C and S2D).

Surprisingly, GO analysis revealed a predominance of MT-associated components in the nucleus, while actin-related proteins were fewer, and intermediate filaments were minimally represented (Figure 1D; Table S1). These included core cytoskeletal components such as gamma-actin (ACTG1), tubulin alpha-8 chain (TUBA8), and vimentin (VIM), as well as many cytoskeleton-associated regulatory proteins and modifiers, including calponin-3 (CNN3) and WD repeat-containing protein 1 (WDR1). To identify proteins of relevance in both species, we focused on the 75 cytoskeleton-associated proteins with high abundance in the nucleus and relatively comparable distribution between nucleus and cytoplasm shared between murine and human NSC samples (Figure 1E; Table S1). Given the overrepresentation of MT-associated proteins (Figure 1D), we prioritized those in the term MT binding (GO:0008017; Table S1), which identified MAP1B, CNN3, MT-associated protein RP/EB family member 1 (MAPRE1), spermatid perinuclear RNA-binding protein (STRBP), RCC2, kinesin-like protein KIF2A, MT-associated protein 2 (MAP2), and mMAP4 (Figure 1E). Among these, MAP1B is the most highly expressed in NSCs (Figure 1F; Table S1), and importantly, 9 distinct MAP1B

(F) Non-zero cell percentage and relative expression (mean expression per gene relative to the maximum and minimum gene expression for NSCs/apical progenitors) for MT binding candidates in NSCs from published publicly available scRNA-seq data.[29]
(G) Mis-sense mutations in *MAP1B* gene identified in patients with PH[30–33]; actin-binding domain (ABD); MT-binding domain (MBD); MT assembly helping domain (MTA); light-chain (LC).
(H) WB images from human iPSC-derived NSCs after subcellular fractionation, stained as indicated.
(I) Orthogonal view of NSCs (PAX6+) from E12 cortical cell cultures depicting the presence of MAP1B inside the nucleus, indicated with arrows.
(J) Representative images of MAP1B intensity in shControl and shMap1b conditions in E12 cortical cell cultures transfected at DIV1 and stained as indicated at DIV3.
(K) MAP1B intensity in the soma and nucleus of cells transfected with either shControl or shMap1b from PAX6+ cells normalized per biological replicate to the average level of MAP1B in control's soma. Two-way ANOVA followed by Šídák's multiple comparisons test. Mean and SEM. Different symbols represent independent cultures. ****$p < 0.0001$.
Scale bars: 50 μm (A), 5 μm (I), and 20 μm (J). DIV, days *in vitro*.
See also Figures S1 and S2.

Please cite this article in press as: Merino et al., Nuclear proteome reveals microtubule-associated protein regulating fate and disease, Cell (2026), https://doi.org/10.1016/j.cell.2026.05.019

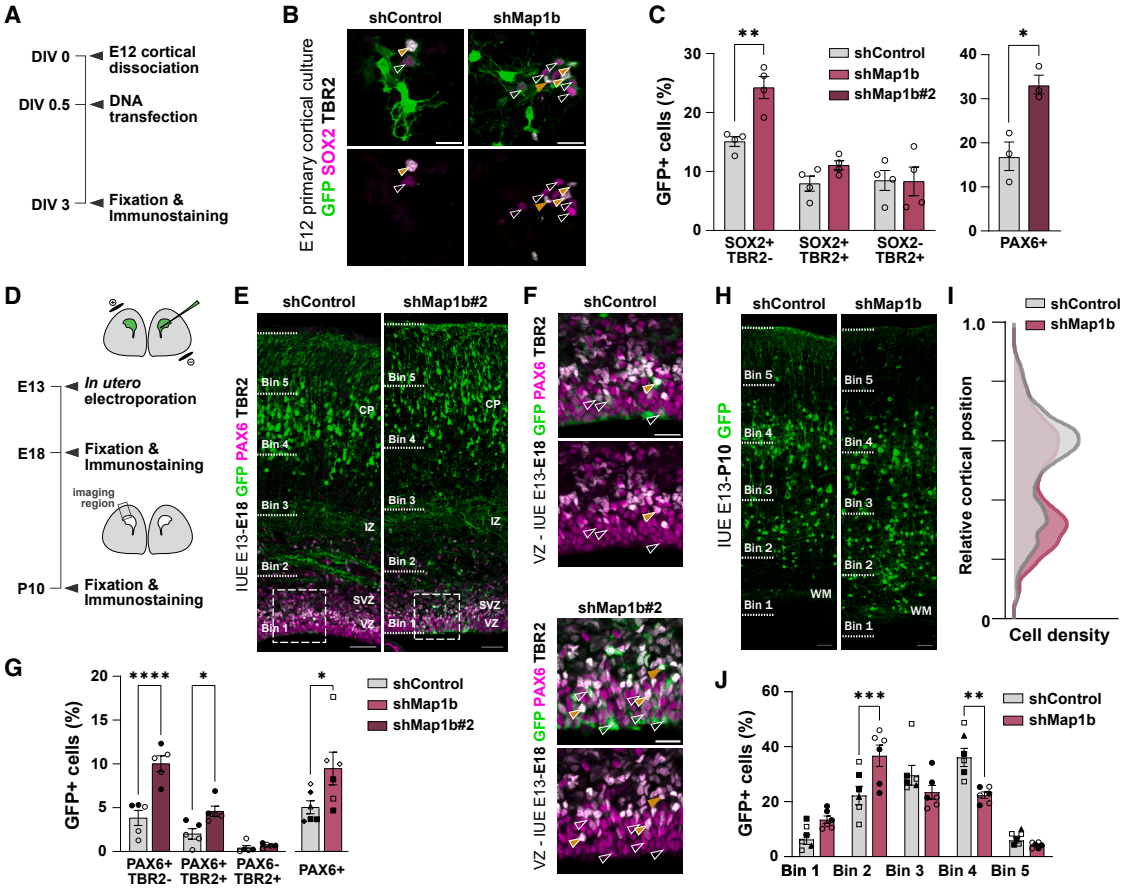

Figure 2. *Map1b* regulates NSC fate

(A) Design of *in vitro* experiments.

(B and C) (B) Representative images of E12 cortical cell cultures transfected with shControl or shMap1b at DIV1 and stained at DIV3 as indicated. The proportion of positive cells are quantified in (C). Mean and SEM. Independent replicates are indicated as dots and tested by two-way ANOVA followed by Šídák's multiple comparisons test (shMap1b) or one-tailed Mann-Whitney test (shMap1b#2).

(D) Design of *in vivo* experiments.

(E–G) (E) Coronal sections of E18 mouse cerebral cortices electroporated at E13 with shControl and shMap1b#2, stained as indicated. Zoom-in images from the VZ and SVZ are shown in (F). Quantification and statistical analysis are shown in (G); two-way ANOVA followed by Šídák's multiple comparisons test (shMap1b#2) or two-tailed Mann-Whitney test (shMap1b).

(H) Coronal sections of P10 mouse cerebral cortices electroporated at E13 with shControl and shMap1b, stained as indicated and quantified in (I) and (J). Two-way ANOVA followed by Šídák's multiple comparisons test. Mean and SEM. Each dot is an animal, and different symbols represent different litters.

Scale bar 20 μm for (B) and (F) and 50 μm for (E) and (H). $^{*}p < 0.05$, $^{**}p < 0.01$, $^{***}p < 0.001$, $^{****}p < 0.0001$. DIV, days *in vitro*; CP, cortical plate; IZ, intermediate zone; SVZ and VZ, (sub) ventricular zone; WM, white matter. White, white and yellow, and yellow arrows indicate GFP+PAX6/SOX2+TBR2−, GFP+PAX6/SOX2+TBR2+, and GFP+PAX6/SOX2−TBR2+ cells, respectively.

See also Figure S3.

mutations have been found in 17 patients presenting bilateral PH (Figures 1G and S2E)—often accompanied by epilepsy and intellectual disability.[33–36] We prioritized MAP1B for functional analysis given its disease relevance and the abscence of studies on MAP1–MAP8 in NSCs.

MAP1B was confirmed in the nucleus and cytoplasm of human and murine NSCs by WB and immunostaining (Figures 1H, 1I, S2C, and S2D). To verify antibody specificity, we generated two distinct short hairpin RNAs (shRNAs) targeting MAP1B, co-expressed with GFP (Figure S2F), both resulting in ∼50% reduction in MAP1B protein levels (Figures S2G–S2L; shMap1b knockdown [KD]: 42.7% ± 6.4% and shMap1b#2 KD: 49.2% ± 6.4%). Immunostaining for MAP1B was significantly reduced in both the cytosol and nucleus in cells expressing *Map1b*-KD constructs, confirming the specificity of the antibody and localization of MAP1B in both compartments (Figures 1J and 1K; soma KD: 53.5% ± 3.1% reduction; nucleus KD: 39.2% ± 3.9% reduction). To explore how the cytoplasmic/nuclear levels of MAP1B change in differentiation, we quantified the nuclear-to-somatic MAP1B ratio in NSCs, intermediate progenitors, and neurons. Notably, the ratio decreased from NSCs to intermediate progenitors and was the lowest in neurons indicating a dynamic distribution shift throughout differentiation (Figures S2M and S2N).

Please cite this article in press as: Merino et al., Nuclear proteome reveals microtubule-associated protein regulating fate and disease, Cell (2026), https://doi.org/10.1016/j.cell.2026.05.019

CellPress
OPEN ACCESS

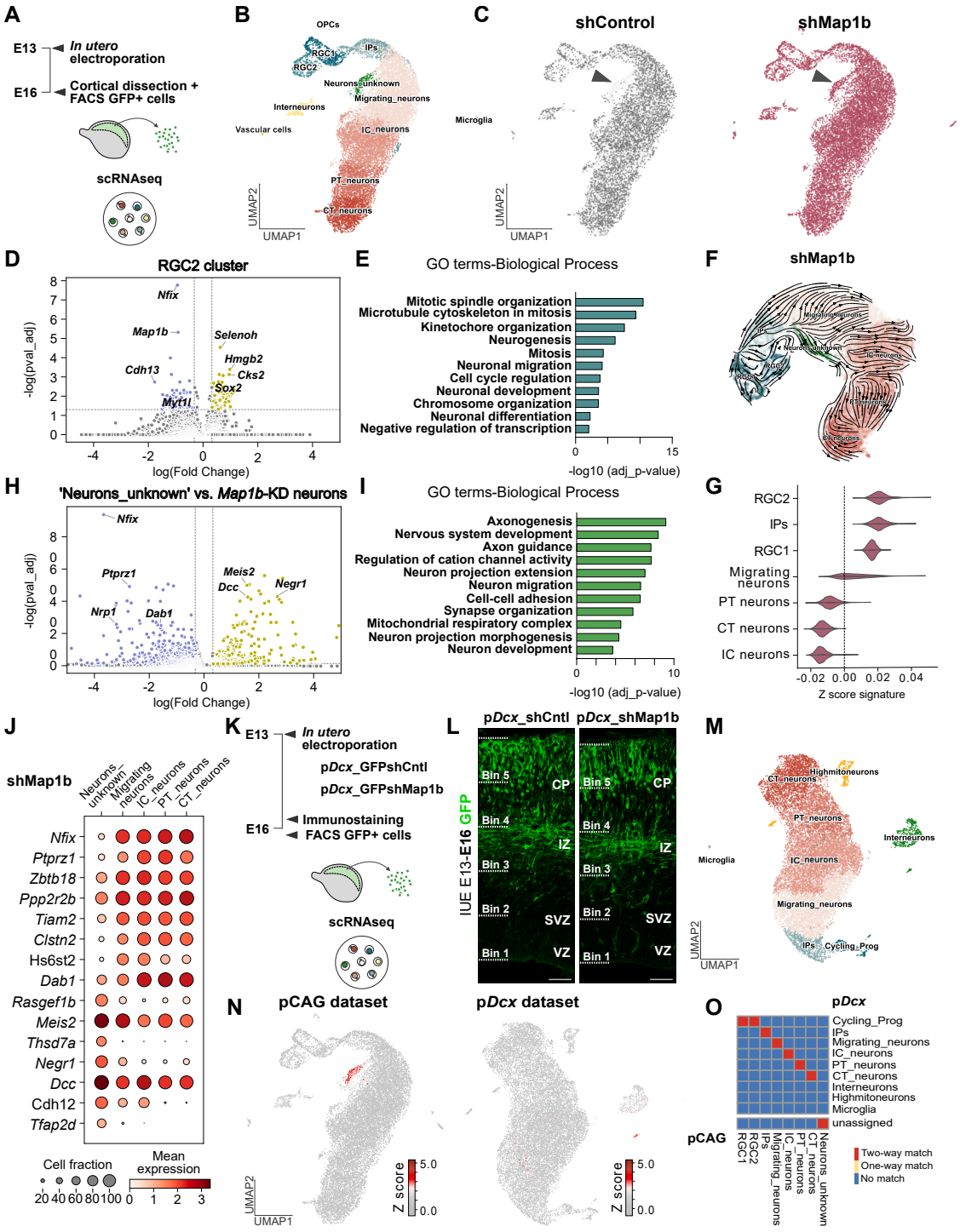

Figure 3. *Map1b*-KD in NSCs generates aberrant neuron population

(A) Experimental design for studying transcriptomic changes upon *Map1b*-KD *in vivo*.

(B) Annotated cell types based on Leiden clustering superimposed on a uniform manifold approximation and projection (UMAP) embedding from both shControl and shMap1b cells.

(C) UMAP embedding from shControl (left) and shMap1b (right) cells.

(D, E, H, and I) Volcano plots from DEG between shControl and shMap1b coming from RGC2 cluster (D) and between Neurons_unknown cluster and all other neurons from *Map1b*-KD (H). Yellow- and violet-colored dots represent upregulated and downregulated genes in the *Map1b*-KD condition for (D) or in the Neurons_unknown cluster for (H). Their main GO terms for biological processes are shown in (E) and (I), respectively.

(legend continued on next page)

Please cite this article in press as: Merino et al., Nuclear proteome reveals microtubule-associated protein regulating fate and disease, Cell (2026), https://doi.org/10.1016/j.cell.2026.05.019

MAP1B regulates NSC fate and cortical development

During neurogenesis and neuronal development, MAP1B has only been studied in neurons, mainly in relation to migration and process formation.[37–41] To explore its function in NSCs independently of migration, we used dissociated cell cultures from the E12 cerebral cortex—the same stage as for the proteome analysis, when the cortex is primarily composed of NSCs.[29] Cells were transfected on the first day of culture with either shControl or shMap1b (Figure 2A), followed by immunostaining for SOX2 to label NSCs and TBR2 to label intermediate progenitors 3 days later (Figure 2B). SOX2+ NSCs were increased upon *Map1b*-KD, compared with control (Figure 2C), a phenotype confirmed with a second shRNA (shMap1b#2) and by a second NSC marker, PAX6 (Figure 2C). To determine if this outcome is due to proliferation, selective cell death, or cell fate changes, cultures were imaged every 15–30 min between 2 and 3 days *in vitro* (DIV) (Figures S3A and S3B; Video S1). Cell survival did not differ between conditions (Figure S3C) nor was proliferation affected, as measured by the proportion of NSCs undergoing mitosis in control vs. KD conditions (Figures S3D and S3E), suggesting that MAP1B regulates NSC fate.

Before exploring the underlying mechanisms, we evaluated this role in regulating NSCs *in vivo* by using *in utero* electroporation (IUE) of *Map1b* shRNAs (shMap1b and shMap1b#2) or shControl at E13, followed by analysis 5 days after (Figure 2D). Immunostaining for PAX6 labeling cortical NSCs and TBR2 for intermediate progenitors (Figures 2E and 2F) showed a significantly higher proportion of PAX6+ NSCs upon *Map1b*-KD for both shRNAs, as compared to control (Figure 2G), confirming that *Map1b*-KD increases NSCs also in the developing cortex *in vivo*.

While the distribution of NSCs was not altered (Figure S3F), we observed a decrease in the proportion of cells reaching the cortical plate upon *Map1b*-KD (Figures S3G–S3I). This could represent a transient phenotype resulting from a higher NSC proportion and a corresponding reduction in neurons. However, at postnatal day 10 (P10), when cortical neurogenesis and neuronal migration are completed, the phenotype is even more pronounced, with a significant number of cells in the lower part of the cortex and a decreased proportion of cells reaching the upper layers (Figures 2H–2J). This was accompanied by a change in neuronal identity, with an increased proportion of CTIP2+ cells following *Map1b*-KD (Figures S3J–S3O). In conclusion, we observed that *Map1b*-KD results in a long-term accumulation of cells in the lower part of the cortex, which resembles the phenotype previously observed in mouse models of PH[27,42] and is consistent with the prediction that MAP1B mutations identified in patients may result in a loss of function[33–36] as modeled here.

Slower NSC differentiation generates an aberrant neuronal population

As *Map1b*-KD leads to more NSCs and deficits in cellular distribution, we performed single-cell RNA sequencing (scRNA-seq) of *Map1b*-KD IUE cells to determine if *Map1b*-KD causes any transcriptional changes and, if so, in which cell types (Figure 3A). After quality control and filtering (see STAR Methods and Figure S4A), a total number of 16,411 cells was obtained. For each litter, we validated the downregulation of *Map1b* (Figure S4B). Notably, expression of other MAPs was not affected by *Map1b*-KD (Figure S4C). Leiden clustering analysis identified all cell types expected in the cortex at this developmental stage[29] (Figures 3B, S4A, and S4D). Yet, one cluster of neurons that predominantly consisted of *Map1b*-KD cells could not be mapped to any known neuronal subtype (cluster "Neurons_unknown"; Figures 3B and 3C).

Given the NSC phenotype described above, we performed differential gene expression (DGE) analysis of stem/progenitor cells between control and *Map1b*-KD. Among these three clusters, the most affected was radial glia cell 2 (RGC2), i.e., differentiating NSCs that already express neuronal and IP markers (Figure 3D; Table S2). The 67 downregulated genes included important inducers of neuronal differentiation (such as *Myt1l* and *Nfix*), while many of the 52 upregulated genes were associated with stemness and proliferation (such as *Sox2* and *Hmgb2*). GO terms for biological processes for these genes comprised mitosis progression and neurogenesis, among others (Figure 3E; Table S2), indicating that *Map1b*-KD promotes NSC stemness also at the gene expression level.

To determine the differentiation trajectory, we used RNA velocity[44] and CellRank,[45] which indicate a likely origin of Neurons_unknown directly from stem/progenitor cells (Figures 3F, 3G, S4E, and S4F), and we identified this cluster as a terminal state in the altered differentiation trajectory (Figure S4G). RGC1 was also identified as a terminal state only upon *Map1b*-KD (Figure S4G), and RNA velocity indicated a higher proportion of cells with slow differentiation pseudo-time in the *Map1b*-KD condition (Figure S4H), revealing a timing difference in progressing through the NSC state.

To explore which genes are most affected in expression in the Neurons_unknown cluster, we performed DGE analysis of this cluster against the rest of the cortical neurons coming from *Map1b*-KD (Figure 3H; Table S2). This identified 657 downregulated and 260 upregulated genes mainly implicated in cell-cell adhesion and neuronal migration (Figures 3I and 3J;

(F) RNA velocity analysis from shMap1b projected in the UMAP, calculated using scVelo.
(G) Violin plots depicting the lineage driver *Z* score signature for Neurons_unknown as a terminal differentiation state per cell type (excluding Neurons_unknown).
(J) Dot plot representing expression of selected DEGs across neuronal populations within *Map1b*-KD treatment.
(K) Experimental design for studying transcriptomic changes upon *Map1b*-KD in neurons.
(L) Coronal sections of E16 mouse cerebral cortices electroporated at E13 with p*Dcx*-driven shControl and shMap1b.
(M) Annotated cell types based on Leiden clustering from both p*Dcx*-driven shControl and shMap1b cells.
(N) Additive *Z* scored gene expression profile of Neurons_unknown across both pCAG and p*Dcx* datasets.
(O) Statistical cluster matching across pCAG and p*Dcx* datasets, using FR-Match.[43]
Scale bar, 50 μm. RGCs, radial glia cells; IPs, intermediate progenitors; IC, intracortical; PT, pyramidal tract; CT, corticothalamic; OPCs, oligodendrocyte progenitor cells; Prog, progenitors; CP, cortical plate; IZ, intermediate zone; SVZ and VZ, (sub) ventricular zone.
See also Figure S4.

Please cite this article in press as: Merino et al., Nuclear proteome reveals microtubule-associated protein regulating fate and disease, Cell (2026), https://doi.org/10.1016/j.cell.2026.05.019

CellPress
OPEN ACCESS

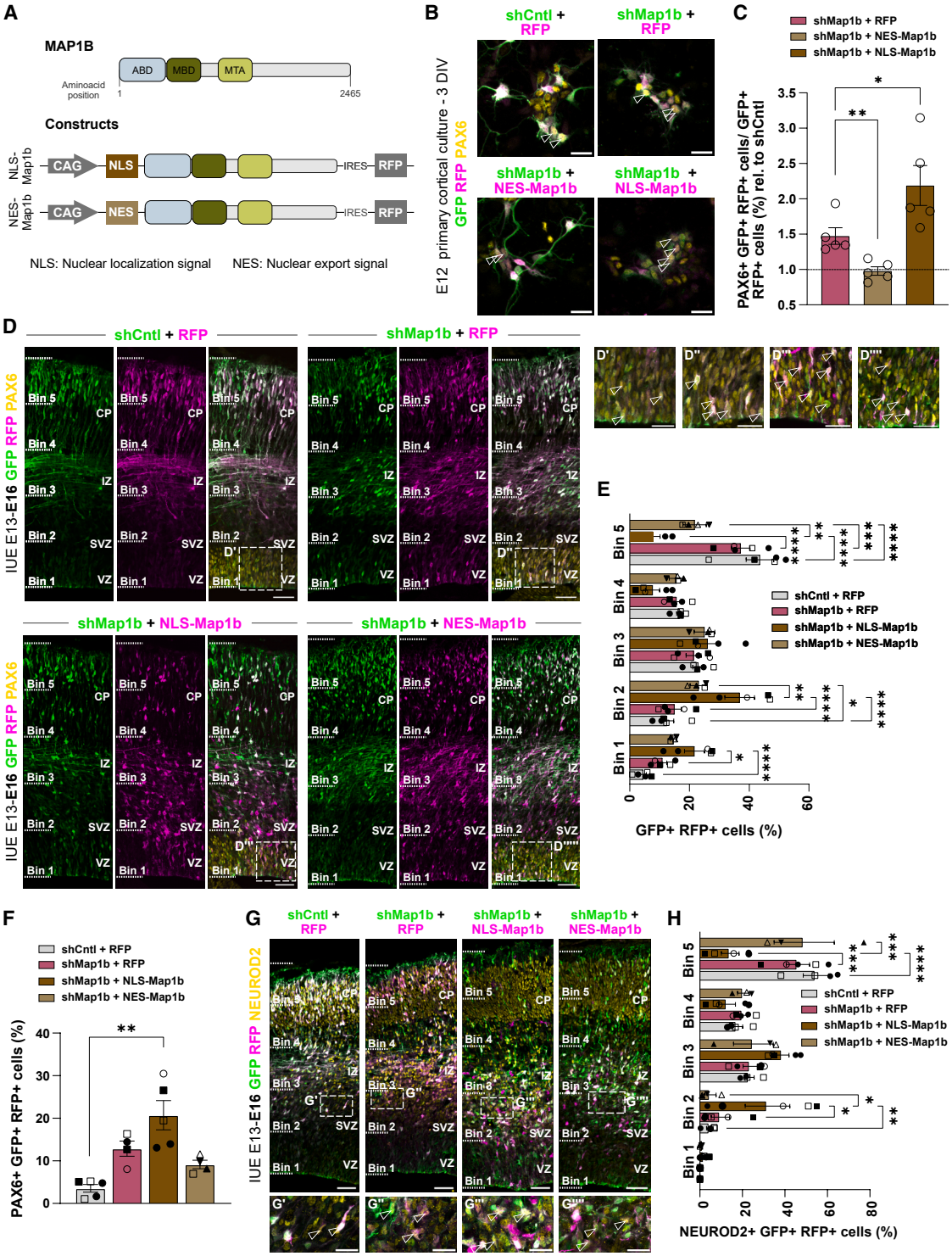

Figure 4. Nuclear MAP1B promotes NSC fate and neuronal ectopia

(A) Schematic DNA constructs used for studying MAP1B subcellular localization in rescue experiments on KD background.

(B) Representative images of E12 cerebral cortex cell cultures transfected at DIV1 and stained at DIV3, as indicated.

(C) Percentage of NSCs (PAX6+ cells) among co-transfected (GFP+/RFP+) cells, relative to shControl+RFP. Paired one-way ANOVA + Greenhouse-Geisser correction followed by Dunnett's multiple comparisons testing.

(legend continued on next page)

Please cite this article in press as: Merino et al., Nuclear proteome reveals microtubule-associated protein regulating fate and disease, Cell (2026), https://doi.org/10.1016/j.cell.2026.05.019

Table S2). These included the downregulation of *Dab1*, which controls neuronal positioning, and *Nrp1*, SEMA3A's receptor regulating the orientation of migrating neurons.[46,47] Importantly, *Map1b* was not among the differentially expressed genes (DEGs), indicating that the presence of this population cannot be attributed to particularly high KD efficiency. The dysregulation of genes involved in axonogenesis, cation channel activity, neuron projection extension, and synapse organization in this cluster (Figure 3I; Table S2) suggests broader deficits in differentiation beyond migration.

The emerging neuronal subpopulation with migration and differentiation deficits is particularly relevant in the context of PH, where not all neurons are affected equally, but rather only a small subpopulation of cells is retained in the periventricular region of the cortex. Interestingly, live imaging of organotypic slices, prepared 2 days after IUE, for approximately 24 h every 15 min, followed by speed and tortuosity (migrated path/straight path) analysis (Figures S4I–S4M; Video S2), revealed a subpopulation of mis-migrating neurons almost exclusively formed by *Map1b*-KD cells (Gaussian mixture models with model section based on minimizing the Bayesian information criterion; Figures S4N–S4Q). These neurons migrated with particularly slow speed and high tortuosity (Figure S4O), validating the emergence of an altered neuronal subpopulation upon *Map1b*-KD.

To discriminate between effects in NSCs and neurons, we restricted *Map1b*-KD to committed progenitors and neurons, using shRNAs under the *Dcx* promoter (p*Dcx*) by IUE (Figure 3K). We did not observe the phenotypes in the distribution of GFP+ cells (Figures 3L and S4R) and in scRNA-seq (Figures 3M and S4S–S4W; e.g., no clusters enriched or depleted in *Map1b*-KD cells) between p*Dcx*-driven *Map1b*-KD and its control. Also, using a *Z* score based on the gene expression signature of the Neurons_unknown cluster, no group of cells with this signature score was detected after p*Dcx*-specific *Map1b*-KD (Figures 3N, S4X, and S4Y), despite the fact that promoter CAG (pCAG) and p*Dcx* datasets were comparable as shown by FR-Match[43] (Figure 3O). In summary, we observed the cellular distribution defects and emergence of an altered neuronal population only upon *Map1b*-KD in NSCs, consistent with a function in regulating NSC fate and neuronal differentiation as also observed *in vitro*.

Nuclear MAP1B promotes NSCs and neuronal ectopia

Given the role of *Map1b* in NSC fate (*in vitro*) and differentiation (*in vivo*), we next sought to understand how MAP1B acts in the different compartments. To determine if and how cytoplasmic and nuclear MAP1B impact NSC fate, we used a molecular substitution approach knocking down endogenous *Map1b* and replacing it with *Map1b* targeted either to the nucleus (by nuclear localization signal [NLS]-Map1b) or to the cytoplasm (by nuclear export signal [NES]-Map1b) (Figures 4A and S5A–S5E). For this, we used shMap1b (Figures S2H and S2I), which targets *Map1b*'s 3′ untranslated region (UTR) to selectively downregulate the endogenous protein while allowing expression of the tagged transfected constructs to explore its effects in the E12 cerebral cortical cell cultures. Quantification of the FLAG-tagged MAP1B revealed 2.5× higher levels in the nucleus for the NLS-Map1b, while NES-Map1b was about 2× enriched in the cytoplasm (Figures S5A and S5B). However, quantifying the total MAP1B levels (KD + rescue by NLS or NES; Figures S5C–S5E) showed that the rescue levels never exceeded the levels of the endogenous MAP1B. Functionally, co-expression of NES-Map1b with shMap1b fully rescued the KD phenotype, reducing the elevated number of NSCs caused by *Map1b*-KD. In contrast, NLS-Map1b exacerbated *Map1b*-KD effects by generating even more NSCs (Figures 4B and 4C). These results indicate that MAP1B nuclear enrichment safeguards NSC identity, while it promotes differentiation in the cytosol, revealing an antagonistic function of MAP1B in the different subcellular compartments.

Given that NLS-Map1b exacerbates the NSC phenotype, we asked whether it would also exacerbate the effects on neuronal positioning *in vivo*. Distribution analysis of GFP+ RFP+ electroporated cells revealed a significant accumulation of the double-positive cells in Bin 1 and Bin 2, with very few cells reaching the upper cortical layers (Bin 5) in the NLS-Map1b condition (containing also RFP and shMap1b co-expressed with *Gfp*), compared with *Map1b*-KD and control (RFP control co-electroporated with shControl or shMap1b co-expressed with *Gfp*) (Figures 4D and 4E). Notably, the proportion of NSCs was significantly increased upon IUE of NLS-Map1b (Figure 4F). Importantly, this was also accompanied by a pronounced accumulation of neurons below the cortical plate (Figures 4G and 4H). Conversely, the NES-Map1b rescue showed no clear differences in NSC proportion and neuronal distribution, compared with control (Figures 4F–4H). However, the cellular distribution was altered with more cells in Bin 2 (Figures 4D and 4E), suggesting that immature neurons (not yet NEUROD2+ as shown in Figure 4H) may exhibit delayed migration. In conclusion, NLS-Map1b exacerbates both NSC maintenance (as observed *in vitro*) and the altered cell distribution phenotype, while NES-Map1b has minor phenotypes *in vivo* with no obvious effect on differentiation.

Brain organoids with PH patient mutations show neuronal ectopia and MAP1B nuclear enrichment

To explore the relevance of the above findings to the predicted loss-of-function MAP1B mutations associated with PH,[33–36]

(D–F) (D) Coronal sections of E16 mouse cerebral cortices electroporated at E13 and stained as indicated and quantified in (E) and (F). Two-way ANOVA followed by Šídák's multiple comparisons test (E) or Kruskal-Wallis test followed by Dunn's multiple comparisons test (F).
(G and H) (G) Coronal sections of E16 mouse cerebral cortices electroporated and stained as indicated and quantified in (H). Two-way ANOVA followed by Šídák's multiple comparisons test.
Scale bar: 20 μm (B, G′, G″, G‴, and G⁗), 50 μm (D and G), and 30 μm (D′, D″, D‴, and D⁗). Mean and SEM; *$p < 0.05$, **$p < 0.01$, ***$p < 0.001$, ****$p < 0.0001$. Each dot is one animal or independent cell culture, and different symbols indicate animals from different litters. White arrows indicate PAX6+GFP+RFP+ cells for (B), (D′), (D″), (D‴) and (D⁗) or NEUROD2+GFP+RFP+ cells for (G′), (G″), (G‴), and (G⁗). DIV, days *in vitro*; NLS, nuclear localization signal; NES, nuclear export signal; ABD, actin-binding domain; MDB, MT-binding domain; MTA, MT assembly helping domain; CP, cortical plate; IZ, intermediate zone; SVZ and VZ, (sub) ventricular zone.
See also Figure S5.

Please cite this article in press as: Merino et al., Nuclear proteome reveals microtubule-associated protein regulating fate and disease, Cell (2026), https://doi.org/10.1016/j.cell.2026.05.019

CellPress
OPEN ACCESS

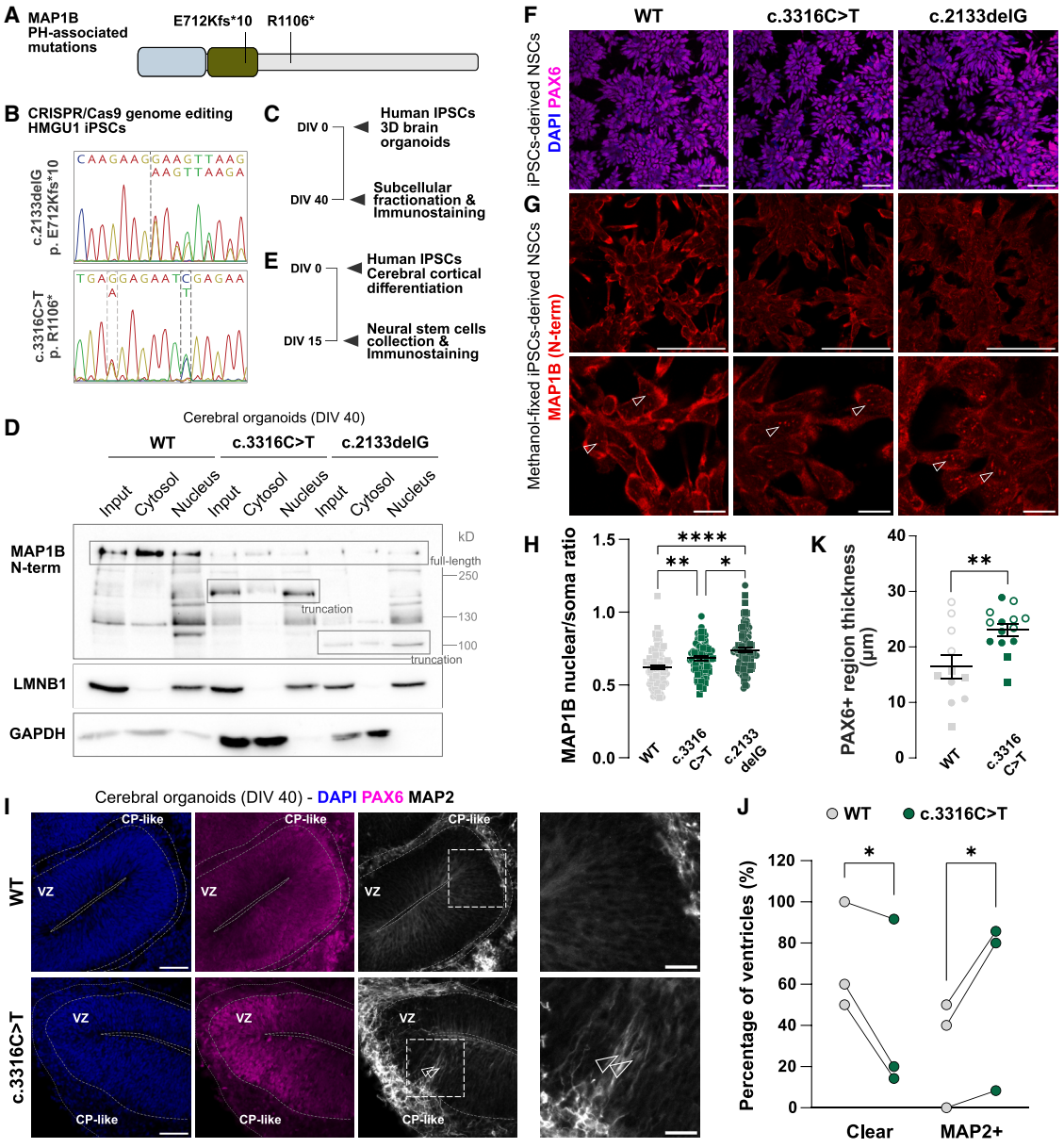

Figure 5. Nuclear-enriched MAP1B isoforms in PH mutant organoids

(A and B) (A) Schematic representation of MAP1B protein structure indicating the two mutations identified in PH patients, introduced in iPSCs by CRISPR-Cas9 as confirmed by Sanger sequencing profile (B).

(C) Experimental design of human iPSC-derived 3D brain organoids.

(D) WB upon subcellular fraction of day 40 organoids from control (WT) and MAP1B mutant lines, stained as indicated.

(E) Experimental design of human iPSC-derived NSCs.

(F) Representative images of iPSC-derived NSC cultures fixed at day 15 and stained as indicated, from control and MAP1B mutant lines.

(G and H) (G) Representative images of iPSC-derived NSC cultures fixed with methanol at day 15 and stained for MAP1B, depicting its cytosolic and nuclear labeling in control and MAP1B mutant lines (nuclear labeling indicated with white arrows) quantified in (H). One-way ANOVA followed by Tukey's multiple comparisons test. Different symbols indicate cells coming from different biological replicates.

(I and J) (I) Representative images of cortical-like structures in day 40 organoids from control (WT) or c.3316C>T mutant depicting the presence of ectopic neurons (MAP2+ cells) in PAX6+ ventricular zones in the mutant, as indicated by white arrows, quantified in (J). *N* = batch; two-way matched ANOVA followed by Fisher's least significant difference test.

(K) Quantification of PAX6+ band thickness in both control (WT) or c.3316C>T mutant organoids. *N* = cortical-like structures, coming from three independent batches, which are indicated by using different symbols. Unpaired two-tailed *t* test.

Scale bar: 50 µm (F, G top, and I left), 10 µm (G, bottom), and 20 µm (I, right); $^{*}p < 0.05$, $^{**}p < 0.01$, $^{****}p < 0.0001$. Mean and SEM. VZ, ventricular zone; CP-like, cortical-plate like.

See also Figure S5.

Please cite this article in press as: Merino et al., Nuclear proteome reveals microtubule-associated protein regulating fate and disease, Cell (2026), https://doi.org/10.1016/j.cell.2026.05.019

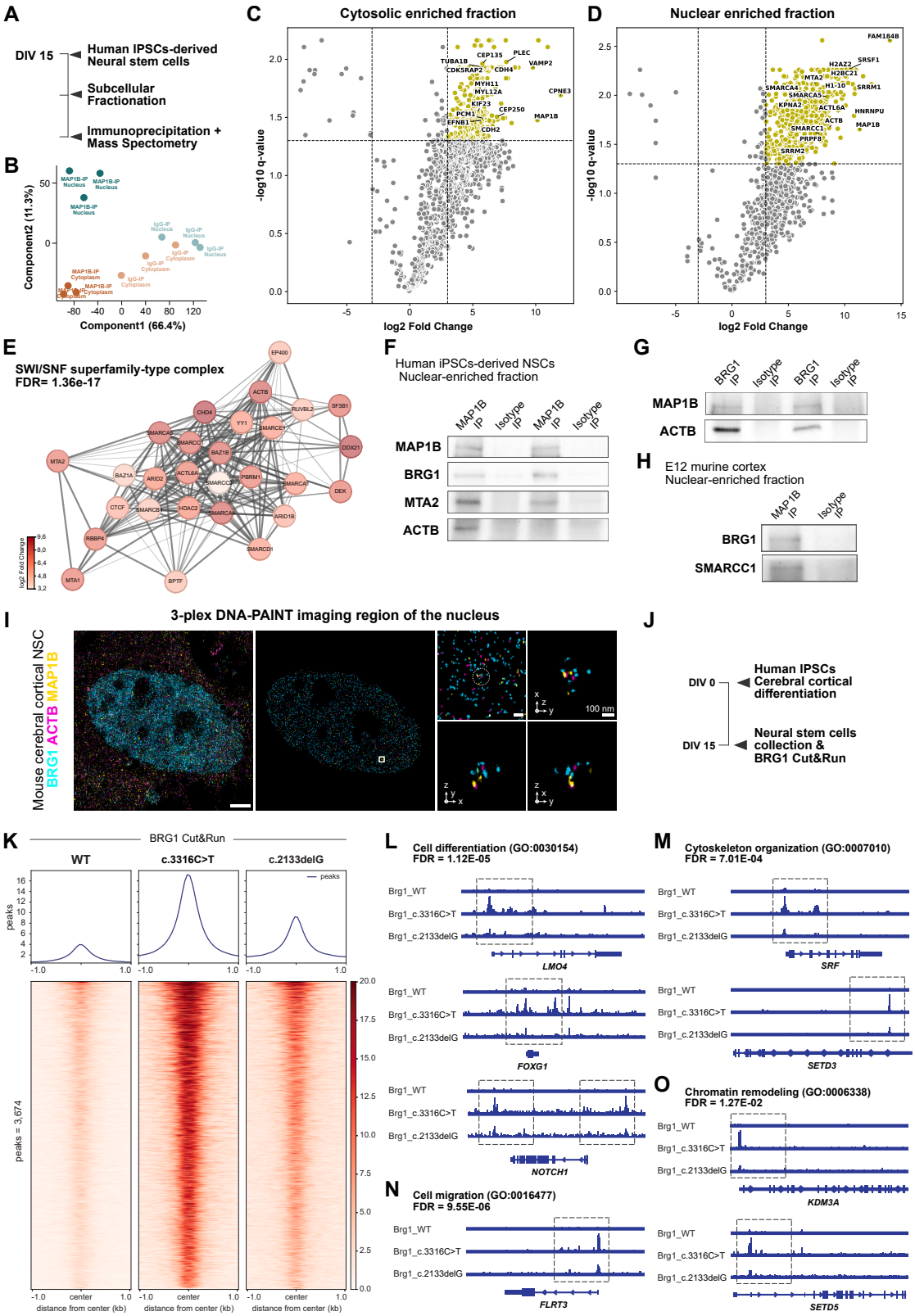

(legend on next page)

Please cite this article in press as: Merino et al., Nuclear proteome reveals microtubule-associated protein regulating fate and disease, Cell (2026), https://doi.org/10.1016/j.cell.2026.05.019

we studied two different mutations with two different approaches. We chose the *MAP1B* c.2133delG; p. E712Kfs*10 and c.3316C>T; p. R1106* mutations (Figure 5A), as both were found in several patients with PH.[33,36] The *MAP1B* c.3316C>T; p. R1106* mutation was originally identified in a patient with bilateral anterior predominant PH and deep perisylvian/insular polymicrogyria, along with collapsing episodes suggestive of seizures.[33] This mutation was inherited from the patient's mother, who presented with similar magnetic resonance imaging (MRI) findings and symptoms. The *MAP1B* c.2133delG; p. E712Kfs*10 mutation was identified in eight members of a family, five of whom presented with PH and intellectual disability.[36]

First, we examined the effects of a MAP1B patient mutation (c.2133delG; p. E712Kfs*10) in the mouse developing cortex using Breasi-CRISPR,[48] i.e., by introducing the patient mutation together with a tag to visualize the mutated protein by IUE (Figure S5F). This showed *MAP1B* c.2133delG; p. E712Kfs*10 mutation resulted in the presence of a truncated MAP1B protein with notably increased nuclear enrichment, as compared with the wild-type (WT)-tagged MAP1B (Figures S5G–S5K). Expression of this mutation also resulted in an abnormal accumulation of cells beneath the cortical plate (Figures S5L–S5O), consistent with a neuronal misplacement phenotype.

Next, we examined the effects of *MAP1B* c.2133delG; p. E712Kfs*10 and c.3316C>T; p. R1106* mutations in human neurodevelopment by generating iPSC lines, using CRISPR without a tag. After confirming the mutations by Sanger sequencing (Figure 5B), we generated brain organoids using as control unedited isogenic iPSCs that underwent the same process (Figure 5C). To determine, if these mutations also result in enrichment in the nucleus as observed in the mouse above (Figures S5I–S5K), subcellular fractionation of the human brain organoids was analyzed by WB for MAP1B. Both mutations resulted in an overall decrease of full-length MAP1B protein (in both nuclear and cytosolic fractions), and each mutant line showed a new MAP1B band at approximately the predicted size of the respective truncated protein (Figure 5D). Most strikingly, both these truncated MAP1B proteins were enriched in the nuclear fraction (Figure 5D). To further corroborate this phenotype, we differentiated the iPSCs into NSCs (Figures 5E and 5F), immunostained them for MAP1B, and quantified its intensity in the soma and nucleus (Figure 5G). This analysis showed significantly higher nuclear/soma levels of the mutants, as compared to WT cells (Figure 5H). Thus, human NSCs harboring patient's mutations reveal a relative nuclear enrichment role of MAP1B, suggesting its possible role in PH pathogenesis.

To further explore pathogenesis, we used the MAP1B c.3316C>T; p. R1106* iPSC line to generate organoids and assess the cortex-like structures. Ectopic neurons (MAP2+ cells) were found in the PAX6+ ventricular zone of the organoids' cortical-like structure in the mutant, but not the control line, in three independent batches (Figures 5I and 5J). Moreover, the thickness of the Pax6+ band was increased in the mutant, compared with control line (Figures 5K, S5P, and S5Q), suggesting a similar bias toward increased NSCs as seen in mice. Thus, the *MAP1B* c.3316C>T; p. R1106* mutation recapitulates the neuronal ectopia phenotype, similar to other proteins mutated in PH patients,[49] and the increased nuclear MAP1B levels along with increased NSCs align with the murine phenotypes described above.

Nuclear MAP1B associates with the BAF chromatin remodeling complex

To further understand MAP1B's function in cell fate, we determined its interactors in human iPSC-derived NSCs by MS upon MAP1B immunoprecipitation (IP) in the above-described fractionation samples (Figures 6A and 6B). Co-immunoprecipitation (coIP) revealed 289 MAP1B interactors in cytosol-enriched samples and 505 MAP1B interactors in nuclear-enriched samples ($\log_2$ fold change > 3 and $q < 0.05$; Figures 6C and 6D; Table S3). Cytosolic interactors include cytoskeletal proteins such as TUBA1B, DNAH3, KIF23, KIF14, CAPZA2, MYL12A, and MYL4, as well as cell adhesion proteins such as EPHA2, CDH2, SEMA4C, NCAM1, and EFNB1 (Table S3)—reflecting the most significant GO terms related to cytoskeleton (Table S3). Notably, among the cytosol-specific interactors, we identified RACGAP1, a GTPase-activating protein that regulates RAC1, CDC42, and RHOA, as observed for MAP1B in other systems.[38] This interaction may explain how MAP1B promotes differentiation when enriched in the cytosol.[1]

GO term analysis of the interactors in the nuclear fraction revealed an overrepresentation of proteins associated with nuclear speckles and chromatin-related processes, including

Figure 6. PH-associated MAP1B mutation increases BAF complex chromatin binding

(A) Experimental design for studying MAP1B's interactors.

(B) Principal components plot for MAP1B interactome in cytosolic-enriched and nuclear-enriched fractions.

(C and D) Volcano plots depicting MAP1B interactome in cytosolic-enriched (C) or nuclear-enriched (D) fractions from human iPSC-derived NSCs.

(E) MAP1B nuclear interactors belonging to the GO term "SWI/SNF superfamily-type complex."

(F–H) WB upon coIP of MAP1B (F and H) or BRG1 (G) from nuclear-enriched fractions derived from human iPSC-derived NSCs (F and G) or E12 mouse cortex (H) and stained as indicated.

(I) DNA-PAINT imaging of BRG1, ACTB, and MAP1B as indicated in a primary culture of murine NSCs. The middle image represents the nuclear segmentation of the cell. Scale bar, 2 μm (left) and 200 nm (middle).

(J) Experimental design for assessing BRG1 function in iPSC-derived NSCs

(K) Enrichment heatmap of BRG1 peaks in Cut&Run analysis from iPSC-derived NSCs generated from WT, MAP1B KI c.3316C>T, and MAP1B KI c.2133delG iPSCs, centered at the middle of the peaks.

(L–O) Peak examples with bigwig profiles associated to genes corresponding to the GO terms cell differentiation (L), cytoskeleton organization (M), cell migration (N), and chromatin remodeling (O).

See also Figures S6 and S7.

Please cite this article in press as: Merino et al., Nuclear proteome reveals microtubule-associated protein regulating fate and disease, Cell (2026), https://doi.org/10.1016/j.cell.2026.05.019

chromatin modifiers and remodelers such as the SWI/SNF superfamily-type BAF complex (Figures 6E and S6A; Table S3). Besides other confirmations (including its association with the nuclear protein importin KPNA2; Figures S6B–S6D), we focused on MAP1B's association with the BAF complex, given its role in regulating NSC fate and neurogenesis.[50–53] CoIP followed by WB confirmed the interaction in both iPSC-derived NSCs and E12 mouse cortical nuclei (Figures 6F–6H). This included BRG1, the core ATPase of the BAF complex, which was further validated by reverse coIP (Figure 6G).

MAP1B has been shown to bind to ACTB,[54] which is also a key component for the BRG1 complex function.[55] We have verified these interactions by IP in the nuclear extract of NSCs (Figures 6F and 6G; Table S3) and probed the spatial vicinity of the three components in the NSC nucleus using super-resolution DNA-PAINT imaging (Figure 6I). Consistently, DNA-PAINT analysis showed nuclear proximity between MAP1B and ACTB in control NSCs, which was affected upon *Map1b*-KD (Figures S6G and S6H). This analysis also confirmed the increased nuclear/soma MAP1B ratio as previously observed by immunofluorescence (Figure S6I). To determine the domain by which MAP1B interacts with BRG1, we expressed FLAG-tagged MAP1B deletion constructs in N2A cells, followed by IP of BRG1 and blotting for FLAG (Figure S6E). This analysis demonstrated that the actin-binding domain of MAP1B is required for the MAP1B-BRG1 interaction (Figures S6E and S6F). Together, these data indicate that MAP1B associates with the nuclear BAF complex in NSCs in an actin-binding-dependent manner.

Considering the relevance of MAP1B subcellular distribution in cell fate outcome, we next explored how this distribution could be regulated. Analysis of MAP1B peptides from our IP proteomes revealed increased phosphorylation in the nuclear fraction (Figures S6J and S6K; Table S3), predicted to be regulated by mitogen-activated protein kinase 8 (MAPK8/JNK1) and/or PTEN-induced putative kinase 1 (PINK1) (Figure S6L; Table S3), previously implicated in MAP1B phosphorylation.[56,57] This is particularly intriguing as phosphorylation weakens the MT interaction of MAPs,[58] potentially facilitating MAP1B nuclear translocation. Using the deletion constructs depicted in Figure S6M, we found that the MT-binding domain (MBD) is involved in nuclear localization, as FLAG-tagged MBD fragments were enriched in the nucleus, whereas other MAP1B truncations remained enriched in the cytoplasm (Figure S6N). These data thus suggest MAP1B subcellular distribution may relate to a phosphorylation-dependent mechanism regulating the nuclear translocation through modulation of MT-binding affinity.

PH-associated MAP1B mutations increase BRG1 chromatin association

Considering the nuclear enrichment of PH-associated MAP1B truncations, we next tested whether patient MAP1B mutations may affect the BAF complex function. For this, we used the iPSC-derived NSCs for BRG1 cleavage under targets and release using nuclease (Cut&Run) on both control and *MAP1B* c.2133delG; p. E712Kfs*10; c.3316C>T; p. R1106* mutants (Figure 6J). In control NSCs, BRG1 shows enrichment at loci associated with cell cycle (*CCND2*, *CCNE1*, *WEE1*) and NSC maintenance (*HMGB2*, *YY1*, *NFYA*), as expected for its role in preserving NSC identity during early neurodevelopment.[59] Strikingly, both MAP1B mutant lines exhibited a marked increase in BRG1 genomic occupancy (Figure 6K), despite comparable BRG1 protein levels across conditions (Figure S7A). This increased chromatin association of BRG1 was recapitulated in day 20 organoids (Figures S7B and S7C). Together, these data suggest that PH-associated MAP1B mutations alter the BAF complex function by enhancing BRG1 chromatin occupancy.

To investigate the biological implications of these changes, we focused on targets shared only between both PH-associated mutant lines, not detected in controls, and performed GO term analysis on the annotated genes associated with these binding peaks (Figure S7D; Table S4). Notably, this analysis uncovered an overrepresentation of transcription factors regulating NSCs—such as *PAX6*, *FOXG1*, *LMO4*, and *NOTCH1*—and chromatin remodeling (as *KDM3A* and *SETD5*), as well as genes associated with cell migration and cytoskeleton organization, such as *FLRT3*, *SRF*, and *SETD3* (Figures 6L–6O). SRF is particularly interesting as its decreased activation mediated by RHOA in the cytoplasm would promote neuronal differentiation,[1] which could be mediated also by MAP1B in the cytoplasm that is known to regulate RHOA activity.[38] In the nucleus, MAP1B can regulate BRG1 binding at *SRF* loci, possibly promoting its transcription given its primary role as transcriptional activator.[60] These results could explain the altered neurodevelopment behind the *MAP1B* mutations, with SRF as a potential common factor in mediating the opposing effects of cytoplasmic and nuclear MAP1B.

DISCUSSION

Here, we explored the nuclear and cytoplasmic proteome of NSCs to identify proteins that had not yet been observed in the nucleus, thereby providing an unbiased resource of potential regulators of cell fate. Our dataset establishes a high-resolution, cross-species resource to identify nuclear and cytoplasmic proteins previously not detected in the respective compartment and thereby elucidate mechanisms and functions in a compartment-specific way. For example, among the most abundant nuclear proteins is a notable overrepresentation of proteins associated with extracellular vesicles (EVs), supporting emerging evidence that EVs translocate into NSC nuclei and modulate gene expression.[61] Conversely, we find enzymes often referred to as histone lysine methyltransferases also in the cytoplasm (Table S1), in line with prior reports,[62,63] expanding the function of these enzymes beyond histone modification. Our proteome highlights the vast and under-appreciated protein diversity present in both major compartments of NSCs, including the abundance of all classes of cytoskeletal proteins within the nuclear compartment.

Importantly, among the significant abundance of various cytoskeletal proteins in the nuclear compartment are many implicated in neurodevelopmental disorders. This raises the intriguing possibility that their nuclear localization—previously unrecognized—could contribute to disease mechanisms, as we found for MAP1B. These include many tubulin isoforms such as TUBB4B and TUBA8, which are linked to tubulinopathies[64,65]

Please cite this article in press as: Merino et al., Nuclear proteome reveals microtubule-associated protein regulating fate and disease, Cell (2026), https://doi.org/10.1016/j.cell.2026.05.019

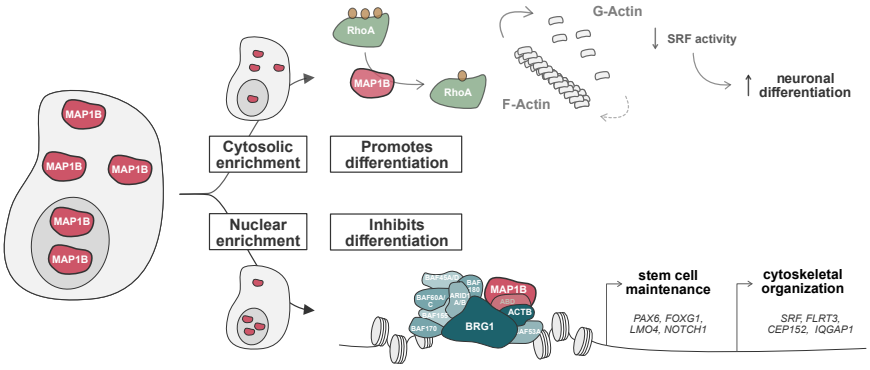

Figure 7. Summary and proposed mechanism for MAP1B subcellular localization leading to opposing functional outcomes

and whose function has so far only been explored in the cytoplasm, or filamin A (FLNA), the most frequently mutated protein in PH.[33,66] Notably, FLNA also interacts with MAP1B in the nucleus, as shown by our interactome in human NSCs. This prompts the hypothesis that FLNA mutations may affect cytoplasmic and nuclear functions contributing to the disease, similar to MAP1B. It is also intriguing that FLNA binds actin, as does MAP1B, and we found the actin-binding domain of MAP1B responsible for interaction with the BRG1 ATPase of the SWI/SNF complex known to comprise ACTB. This highlights the potential nuclear contribution of these actin-binding proteins in fate decisions in the nucleus and hence challenges the current view on the etiology of PH considered solely as "migration disorders." Our data demonstrate that the disease originates in NSCs, as manipulating MAP1B or other PH mutations[7] in neurons only does not lead to any neuronal ectopia. This suggests that the delay in NSC differentiation leads to changes in neurons incompatible with reaching their normal position. In line with this, we demonstrate that most, if not all, MAP1B-KD neurons migrate more slowly, but only a subset migrates at the slowest speed and along the most curved paths. This is consistent with a subgroup of neurons exhibiting transcriptional alterations and fate changes, further supported by our data pointing to a cell-autonomous mechanism (Figures S7E–S7G). Taken together, these data propose to revise the concept of PH as a sole migration disorder to a "fate disorder," arising at NSC state and causing the strongest deficits in a subgroup of neurons.

Using MAP1B as proof of functional relevance, we show that its cytoplasmic/nuclear ratio has a profound impact on neurodevelopment, with its cytoplasmic depletion and nuclear enrichment prolonging NSC fate and leading to neuronal ectopia. Consistently, in the MAP1B-KD condition, we observed an increased nucleus-to-soma MAP1B ratio, associated with an increase in NSC fate. This shift may result from a preferential depletion of the cytoplasmic pool (e.g., if nuclear MAP1B is more stable) or from a redistribution toward the nucleus upon KD. Functionally, the KD could favor NSC fate by relatively increasing nuclear MAP1B levels (as compared with the cytosol) and/or by preferentially reducing its pro-differentiation cytoplasmic activity. Importantly, we found that such a depletion of full-length MAP1B and nuclear enrichment of the mutant-truncated MAP1B are present in human patients with (heterozygous) MAP1B mutations. Thus, both murine and human patient data support a model in which reduced cytoplasmic function of MAP1B and its increased nuclear function—as demonstrated by increase binding of the BRG1 subunit of the SWI/SNF (BAF) chromatin remodeling complex to its targets—slow NSC differentiation driving neuronal ectopia. The unbiased MAP1B interactome revealed a possible mechanism for this based on its association with the SWI/SNF (BAF) chromatin remodeling complex that has been implicated in NSC fate.[50–52,59] Two different PH-associated MAP1B mutations increase BRG1 binding genome-wide, particularly at genes promoting NSC fate and regulating migration, supporting MAP1B as an integrator of cytoskeletal dynamics and fate decisions. Mechanistically, we identified that the MBD and the phosphorylation status affect the shuttling to the nucleus and that the actin-binding domain interacts with BRG1. Thus, MAP1B may link the complex to actin and, depending on MAP1B nuclear levels, may thereby modulate the BAF complex binding to target sites (Figure 7).

Our results not only uncover a mechanism by which a cytoskeletal protein regulates cell fate in NSCs but also reveal an intriguing case with subcellular localization leading to opposing functional outcomes; driving MAP1B to the cytoplasm promotes neuronal differentiation, while its nuclear enrichment results in the opposite phenotype. Our evidence indicates that actin regulation could mediate the effects in both cellular compartments (Figure 7). This compartment-specific antagonism provides a fast and adaptable mechanism for regulating NSC fate via shifts in the cytoplasmic-to-nuclear ratio of MAP1B. Importantly, this concept may generally apply to other proteins with this abundance and distribution revealed in our proteome, and it offers a rich resource to identify more such proteins and similar mechanisms in other stem cells.

Together, our findings uncover a function of MAP1B as fate regulator and highlight a broader paradigm in which cytoskeleton-associated proteins can dynamically translocate into the nucleus to regulate transcriptional programs and stem cell fate. This opens future directions for studying how subcellular localization of proteins can impact cell function and their implications in human disease.

Limitations of the study

While we detected and functionally focused on full-length MAP1B, we did not determine whether additional MAP1B isoforms are present or contribute to compartment-specific functions. Moreover, the ideal method to determine the compartment-specific function of MAP1B would be to delete endogenous MAP1B selectively in one compartment. This could either be done by mutating the respective phosphorylation sites, but they seem to be many and would also affect cytoplasmic function. Another approach could be to use degron

technology and apply, for example, light-inducible degradation approaches. However, MAP1B may immediately shuttle back to the nucleus, impairing the analysis of changes in cell fate that require longer-term persistent manipulations. We therefore think that the approach applied here to target MAP1B to the nucleus (by NLS) or the cytoplasm (by NES) on the background of the KD condition, thereby never exceeding WT levels, is presently the best available. In addition, we found that detection of MAP1B in the nucleus by immunostaining was sensitive to fixation conditions, including fixation time and fixative used, which may result in variability between experiments and explain why MAP1B's nuclear localization had been missed before.

RESOURCE AVAILABILITY

Lead contact

Further information and requests for resources and reagents should be directed to the lead contact, Magdalena Götz (magdalena.goetz@helmholtz-munich.de).

Materials availability

All unique/stable reagents and human iPSC lines generated in this study are available from the lead contact with a completed materials transfer agreement.

Data and code availability

- Proteomics, scRNA-seq, and Cut&Run data have been deposited to the ProteomeXchange Consortium via the PRIDE[67] partner repository and BioStudies, with the accession numbers listed in the key resources table.
- This paper does not report original code.
- Any additional information required to reanalyze the data reported in this paper is available from the lead contact upon request.

ACKNOWLEDGMENTS

We thank Ines Muehlhahn and Paulina Chlebik for excellent technical help, Tatiana Simon and Judith Fischer for their excellent assistance with single-cell sequencing experiments, and Daniela Cimino and Fabio Lateef Laredo for important experiments that could not be included in the manuscript for reasons of space. We are also very grateful for the excellent characterization of the iPSC lines by Ejona Rusha from the Core Facility Induced Pluripotent Stem Cells, and we acknowledge the Core facility Genomics of the Helmholtz Center Munich, the Laboratory for Functional Genome Analysis (LAFUGA) of Gene Center Munich, and the Flow Cytometry and Imaging Facility of the Biomedical Center of Munich for providing equipment, services, and expertise. We are particularly grateful to Laurent Nguyen, Antonela Bonafina, and Julie Stoufflet for generously sharing their expertise and teaching us the live imaging used in this study. We also thank Christoph Gruber for sharing the nuclear export/localization signal sequences. We are also grateful to Jovica Ninkovic and Stefan Stricker and the Götz lab for their valuable input throughout all phases of the project. This work was supported by the European Research Council (advanced grant NeuroCentro, 885382 to M.G.; consolidator Grant ExoDevo, 101043959 to S.C.) and the German Excellence Cluster SyNergy (EXC2145/project-ID 390857198, to M.G.). L.M. is supported by the European Union's Horizon 2020 research and innovation programme under the Marie Skłodowska-Curie PhD grant agreement no. 813533. Parts of this work were funded by a New Frontiers in Research Fund Transformation grant to M.G., funded through three Canadian Federal Agencies (CIHR, NSERC, and SSHRC).

AUTHOR CONTRIBUTIONS

Conceptualization, M.G. and F.M.; methodology, F.M., L.M., A.K., Y.L., J.M.-P., E.-M.S., C.S., F.G., B.A.H., M.B., and V.P.; investigation, F.M., A.K., J.F.B., L.-J.P., D.K.S., and C.K.; writing—original draft, F.M. and M.G.; writing—review and editing, F.M. and M.G. with suggestions from most co-authors; funding acquisition, M.G. and S.C.; and supervision, S.M.H., S.C., R.J., L.-J.P., and M.G.

DECLARATION OF INTERESTS

M.G. is a member of the advisory board of *Cell*.

DECLARATION OF GENERATIVE AI AND AI-ASSISTED TECHNOLOGIES IN THE WRITING PROCESS

During the preparation of this work, the authors used ChatGPT to assist with grammatical revision. After using this tool, the authors reviewed and edited the content as needed and take full responsibility for the content of the publication.

STAR★METHODS

Detailed methods are provided in the online version of this paper and include the following:

- KEY RESOURCES TABLE
- EXPERIMENTAL MODEL AND STUDY PARTICIPANT DETAILS
  - Experimental animals
  - Primary cerebral cortical cultures
  - Neuro2A cells
  - Human induced pluripotent stem cells
  - iPSC-derived dorsal forebrain neural stem cells
  - Cerebral organoids
- METHOD DETAILS
  - In utero electroporation (IUE)
  - Primary cortical cultures preparation
  - Generation of mutant iPSCs
  - IPSC-derived dorsal forebrain neural stem cells differentiation
  - Generation of cerebral organoids
  - Recombinant DNA cloning
  - Breasi-CRISPR
  - Cell transfection
  - Immunostaining
  - Protein extraction
  - Immunoprecipitation
  - Mass spectrometry
  - Western blot
  - Live imaging
  - Fluorescence-activated cell sorting (FACS)
  - Single-cell transcriptomics
  - Cut and Run
  - DNA-paint
  - Recombinant DNA
  - shRNA sequences
  - Docking site sequences
  - Experimental parameters for DNA-PAINT imaging
- QUANTIFICATION AND STATISTICAL ANALYSIS

SUPPLEMENTAL INFORMATION

Supplemental information can be found online at https://doi.org/10.1016/j.cell.2026.05.019.

Received: November 14, 2024
Revised: February 18, 2026
Accepted: May 14, 2026

REFERENCES

1. Cossard, A., Stam, K., Smets, A., and Jossin, Y. (2023). MKL/SRF and Bcl6 mutual transcriptional repression safeguards the fate and

positioning of neocortical progenitor cells mediated by RhoA. Sci. Adv. *9*, eadd0676. https://doi.org/10.1126/sciadv.add0676.

2. Driskill, J.H., and Pan, D. (2023). Control of stem cell renewal and fate by YAP and TAZ. Nat. Rev. Mol. Cell Biol. *24*, 895–911. https://doi.org/10.1038/s41580-023-00644-5.
3. Dupont, S., Morsut, L., Aragona, M., Enzo, E., Giulitti, S., Cordenonsi, M., Zanconato, F., Le Digabel, J., Forcato, M., Bicciato, S., et al. (2011). Role of YAP/TAZ in mechanotransduction. Nature *474*, 179–183. https://doi.org/10.1038/nature10137.
4. Connelly, J.T., Gautrot, J.E., Trappmann, B., Tan, D.W.M., Donati, G., Huck, W.T.S., and Watt, F.M. (2010). Actin and serum response factor transduce physical cues from the microenvironment to regulate epidermal stem cell fate decisions. Nat. Cell Biol. *12*, 711–718. https://doi.org/10.1038/ncb2074.
5. Merino, F., and Götz, M. (2025). The role of moonlighting proteins in neurogenesis. Curr. Opin. Neurobiol. *93*, 103047. https://doi.org/10.1016/j.conb.2025.103047.
6. Sigaeva, A., Hutchings, C., Cesnik, A., Lilley, K.S., and Lundberg, E. (2026). Subcellular localization as a driver of protein function. Nat. Rev. Mol. Cell Biol. https://doi.org/10.1038/s41580-026-00947-3.
7. O'Neill, A.C., Uzbas, F., Antognolli, G., Merino, F., Draganova, K., Jäck, A., Zhang, S., Pedini, G., Schessner, J.P., Cramer, K., et al. (2022). Spatial centrosome proteome of human neural cells uncovers disease-relevant heterogeneity. Science *376*, eabf9088. https://doi.org/10.1126/science.abf9088.
8. Wheway, G., Schmidts, M., Mans, D.A., Szymanska, K., Nguyen, T.T., Racher, H., Phelps, I.G., Toedt, G., Kennedy, J., Wunderlich, K.A., et al. (2015). An siRNA-based functional genomics screen for the identification of regulators of ciliogenesis and ciliopathy genes. Nat. Cell Biol. *17*, 1074–1087. https://doi.org/10.1038/ncb3201.
9. Busselez, J., Uzbekov, R.E., Franco, B., and Pancione, M. (2023). New insights into the centrosome-associated spliceosome components as regulators of ciliogenesis and tissue identity. Wiley Interdiscip. Rev. RNA *14*, e1776. https://doi.org/10.1002/wrna.1776.
10. Kumeta, M., Yoshimura, S.H., Hejna, J., and Takeyasu, K. (2012). Nucleocytoplasmic shuttling of cytoskeletal proteins: Molecular mechanism and biological significance. Int. J. Cell Biol. *2012*, 494902. https://doi.org/10.1155/2012/494902.
11. Ludueña, R.F., Walss-Bass, C., Portyanko, A., Guo, J., and Yeh, I.T. (2022). Nuclear βII-Tubulin and its Possible Utility in Cancer Diagnosis, Prognosis and Treatment. Front. Cell Dev. Biol. *10*, 870088. https://doi.org/10.3389/fcell.2022.870088.
12. Akoumianaki, T., Kardassis, D., Polioudaki, H., Georgatos, S.D., and Theodoropoulos, P.A. (2009). Nucleocytoplasmic shuttling of soluble tubulin in mammalian cells. J. Cell Sci. *122*, 1111–1118. https://doi.org/10.1242/jcs.043034.
13. Obrdlik, A., and Percipalle, P. (2011). The F-actin severing protein cofilin-1 is required for RNA polymerase II transcription elongation. Nucleus *2*, 72–79. https://doi.org/10.4161/nucl.2.1.14508.
14. Xie, X., Mahmood, S.R., Gjorgjieva, T., and Percipalle, P. (2020). Emerging roles of cytoskeletal proteins in regulating gene expression and genome organization during differentiation. Nucleus *11*, 53–65. https://doi.org/10.1080/19491034.2020.1742066.
15. Xie, X., Jankauskas, R., Mazari, A.M.A., Drou, N., and Percipalle, P. (2018). β-actin regulates a heterochromatin landscape essential for optimal induction of neuronal programs during direct reprograming. PLoS Genet. *14*, e1007846. https://doi.org/10.1371/journal.pgen.1007846.
16. Hofmann, W.A., Stojiljkovic, L., Fuchsova, B., Vargas, G.M., Mavrommatis, E., Philimonenko, V., Kysela, K., Goodrich, J.A., Lessard, J.L., Hope, T.J., et al. (2004). Actin is part of pre-initiation complexes and is necessary for transcription by RNA polymerase II. Nat. Cell Biol. *6*, 1094–1101. https://doi.org/10.1038/ncb1182.
17. Percipalle, P., and Vartiainen, M. (2019). Cytoskeletal proteins in the cell nucleus: A special nuclear actin perspective. Mol. Biol. Cell *30*, 1781–1785. https://doi.org/10.1091/mbc.E18-10-0645.
18. Percipalle, P., Fomproix, N., Kylberg, K., Miralles, F., Bjorkroth, B., Daneholt, B., and Visa, N. (2003). An actin-ribonucleoprotein interaction is involved in transcription by RNA polymerase II. Proc. Natl. Acad. Sci. USA *100*, 6475–6480. https://doi.org/10.1073/pnas.1131933100.
19. Sharili, A.S., Kenny, F.N., Vartiainen, M.K., and Connelly, J.T. (2016). Nuclear actin modulates cell motility via transcriptional regulation of adhesive and cytoskeletal genes. Sci. Rep. *6*, 33893. https://doi.org/10.1038/srep33893.
20. Chan, C.J., Heisenberg, C.P., and Hiiragi, T. (2017). Coordination of morphogenesis and cell-fate specification in development. Curr. Biol. *27*, R1024–R1035. https://doi.org/10.1016/j.cub.2017.07.010.
21. Sivakumar, A., and Kurpios, N.A. (2018). Transcriptional regulation of cell shape during organ morphogenesis. J. Cell Biol. *217*, 2987–3005. https://doi.org/10.1083/jcb.201612115.
22. Francis, F., and Cappello, S. (2021). Neuronal migration and disorders – an update. Curr. Opin. Neurobiol. *66*, 57–68. https://doi.org/10.1016/j.conb.2020.10.002.
23. Watrin, F., Manent, J.B., Cardoso, C., and Represa, A. (2015). Causes and consequences of gray matter heterotopia. CNS Neurosci. Ther. *21*, 112–122. https://doi.org/10.1111/cns.12322.
24. Vriend, I., and Oegema, R. (2021). Genetic causes underlying grey matter heterotopia. Eur. J. Paediatr. Neurol. *35*, 82–92. https://doi.org/10.1016/j.ejpn.2021.09.015.
25. Severino, M., Geraldo, A.F., Utz, N., Tortora, D., Pogledic, I., Klonowski, W., Triulzi, F., Arrigoni, F., Mankad, K., Leventer, R.J., et al. (2020). Definitions and classification of malformations of cortical development: Practical guidelines. Brain *143*, 2874–2894. https://doi.org/10.1093/brain/awaa174.
26. Lian, G., Wong, T., Lu, J., Hu, J., Zhang, J., and Sheen, V. (2019). Cytoskeletal associated filamin a and RhoA affect neural progenitor specification during mitosis. Cereb. Cortex *29*, 1280–1290. https://doi.org/10.1093/cercor/bhy033.
27. Cappello, S., Gray, M.J., Badouel, C., Lange, S., Einsiedler, M., Srour, M., Chitayat, D., Hamdan, F.F., Jenkins, Z.A., Morgan, T., et al. (2013). Mutations in genes encoding the cadherin receptor-ligand pair DCHS1 and FAT4 disrupt cerebral cortical development. Nat. Genet. *45*, 1300–1308. https://doi.org/10.1038/ng.2765.
28. Lian, G., Lu, J., Hu, J., Zhang, J., Cross, S.H., Ferland, R.J., and Sheen, V.L. (2012). Filamin a regulates neural progenitor proliferation and cortical size through wee1-dependent Cdk1 phosphorylation. J. Neurosci. *32*, 7672–7684. https://doi.org/10.1523/JNEUROSCI.0894-12.2012.
29. Di Bella, D.J., Habibi, E., Stickels, R.R., Scalia, G., Brown, J., Yadollahpour, P., Yang, S.M., Abbate, C., Biancalani, T., Macosko, E.Z., et al. (2021). Molecular logic of cellular diversification in the mouse cerebral cortex. Nature *595*, 554–559. https://doi.org/10.1038/s41586-021-03670-5.
30. Dopie, J., Skarp, K.-P., Rajakylä, E.K., Tanhuanpää, K., and Vartiainen, M.K. (2012). Active maintenance of nuclear actin by importin 9 supports transcription. Proc. Natl. Acad. Sci. USA *109*, E544–E552. https://doi.org/10.1073/pnas.1118880109.
31. Yokoya, F., Imamoto, N., Tachibana, T., and Yoneda, Y. (1999). β-Catenin can be transported into the nucleus in a Ran-unassisted manner. Mol. Biol. Cell *10*, 1119–1131. https://doi.org/10.1091/mbc.10.4.1119.
32. Lui, K., and Huang, Y. (2009). RanGTPase: A Key Regulator of Nucleocytoplasmic Trafficking. Mol. Cell. Pharmacol. *1*, 148–156. https://doi.org/10.4255/mcpharmacol.09.19.
33. Heinzen, E.L., O'Neill, A.C., Zhu, X., Allen, A.S., Bahlo, M., Chelly, J., Chen, M.H., Dobyns, W.B., Freytag, S., Guerrini, R., et al. (2018). De novo and inherited private variants in MAP1B in periventricular nodular

heterotopia. PLoS Genet. *14*, e1007281. https://doi.org/10.1371/journal.pgen.1007281.

34. Julca, D.M., Diaz, J., Berger, S., and Leon, E. (2019). MAP1B related syndrome: Case presentation and review of literature. Am. J. Med. Genet., A *179*, 1703–1708. https://doi.org/10.1002/ajmg.a.61280.

35. Arya, R., Spaeth, C., and Zhang, W. (2021). Epilepsy phenotypes associated with MAP1B-related brain malformations. Epileptic Disord. *23*, 392–396. https://doi.org/10.1684/epd.2021.1258.

36. Walters, G.B., Gustafsson, O., Sveinbjornsson, G., Eiriksdottir, V.K., Agustsdottir, A.B., Jonsdottir, G.A., Steinberg, S., Gunnarsson, A.F., Magnusson, M.I., Unnsteinsdottir, U., et al. (2018). MAP1B mutations cause intellectual disability and extensive white matter deficit. Nat. Commun. *9*, 3456. https://doi.org/10.1038/s41467-018-05595-6.

37. Takei, Y., Teng, J., Harada, A., and Hirokawa, N. (2000). Defects in Axonal Elongation and Neuronal Migration in Mice with Disrupted tau and map1b Genes. J. Cell Biol. *150*, 989–1000. https://doi.org/10.1083/jcb.150.5.989.

38. Montenegro-Venegas, C., Tortosa, E., Rosso, S., Peretti, D., Bollati, F., Bisbal, M., Jausoro, I., Avila, J., Cáceres, A., and Gonzalez-Billault, C. (2010). MAP1B Regulates Axonal Development by Modulating Rho-GTPase Rac1 Activity. Mol. Biol. Cell *21*, 3518–3528. https://doi.org/10.1091/mbc.e09-08-0709.

39. González-Billault, C., Del Río, J.A., Ureña, J.M., Jiménez-Mateos, E.M., Barallobre, M.J., Pascual, M., Pujadas, L., Simó, S., Torre, A.L., Gavin, R., et al. (2005). A role of MAP1B in reelin-dependent neuronal migration. Cereb. Cortex *15*, 1134–1145. https://doi.org/10.1093/cercor/bhh213.

40. Gonzalez-Billault, C., Avila, J., and Cáceres, A. (2001). Evidence for the Role of MAP1B in Axon Formation. Mol. Biol. Cell *12*, 2087–2098. https://doi.org/10.1091/mbc.12.7.2087.

41. Messaoudi, S., Allam, A., Stoufflet, J., Paillard, T., Le Ven, A., Fouquet, C., Doulazmi, M., Trembleau, A., and Caille, I. (2024). FMRP regulates postnatal neuronal migration via MAP1B. eLife *12*, RP88782. https://doi.org/10.7554/eLife.88782.

42. Broix, L., Jagline, H., Ivanova, E., Schmucker, S., Drouot, N., Clayton-Smith, J., Pagnamenta, A.T., Metcalfe, K.A., Isidor, B., Louvier, U.W., et al. (2016). Mutations in the HECT domain of NEDD4L lead to AKT-mTOR pathway deregulation and cause periventricular nodular heterotopia. Nat. Genet. *48*, 1349–1358. https://doi.org/10.1038/ng.3676.

43. Zhang, Y., Aevermann, B., Gala, R., and Scheuermann, R.H. (2022). Cell type matching in single-cell RNA-sequencing data using FR-Match. Sci. Rep. *12*, 9996. https://doi.org/10.1038/s41598-022-14192-z.

44. Bergen, V., Lange, M., Peidli, S., Wolf, F.A., and Theis, F.J. (2020). Generalizing RNA velocity to transient cell states through dynamical modeling. Nat. Biotechnol. *38*, 1408–1414. https://doi.org/10.1038/s41587-020-0591-3.

45. Lange, M., Bergen, V., Klein, M., Setty, M., Reuter, B., Bakhti, M., Lickert, H., Ansari, M., Schniering, J., Schiller, H.B., et al. (2022). CellRank for directed single-cell fate mapping. Nat. Methods *19*, 159–170. https://doi.org/10.1038/s41592-021-01346-6.

46. Franco, S.J., Martinez-Garay, I., Gil-Sanz, C., Harkins-Perry, S.R., and Müller, U. (2011). Reelin Regulates Cadherin Function via Dab1/Rap1 to Control Neuronal Migration and Lamination in the Neocortex. Neuron *69*, 482–497. https://doi.org/10.1016/j.neuron.2011.01.003.

47. Chen, G., Sima, J., Jin, M., Wang, K.Y., Xue, X.J., Zheng, W., Ding, Y.Q., and Yuan, X.B. (2008). Semaphorin-3A guides radial migration of cortical neurons during development. Nat. Neurosci. *11*, 36–44. https://doi.org/10.1038/nn2018.

48. Meyerink, B.L., Kc, P., Tiwari, N.K., Kittock, C.M., Klein, A., Evans, C.M., and Pilaz, L.J. (2022). Breasi-CRISPR: an efficient genome-editing method to interrogate protein localization and protein-protein interactions in the embryonic mouse cortex. Development *149*, dev200616. https://doi.org/10.1242/dev.200616.

49. Klaus, J., Kanton, S., Kyrousi, C., Ayo-Martin, A.C., Di Giaimo, R., Riesenberg, S., O'Neill, A.C., Camp, J.G., Tocco, C., Santel, M., et al. (2019). Altered neuronal migratory trajectories in human cerebral organoids derived from individuals with neuronal heterotopia. Nat. Med. *25*, 561–568. https://doi.org/10.1038/s41591-019-0371-0.

50. Son, E.Y., and Crabtree, G.R. (2014). The role of BAF (mSWI/SNF) complexes in mammalian neural development. Am. J. Med. Genet., C *166C*, 333–349. https://doi.org/10.1002/ajmg.c.31416.

51. Sokpor, G., Xie, Y., Rosenbusch, J., and Tuoc, T. (2017). Chromatin remodeling BAF (SWI/SNF) complexes in neural development and disorders. Front. Mol. Neurosci. *10*, 243. https://doi.org/10.3389/fnmol.2017.00243.

52. Braun, S.M.G., Petrova, R., Tang, J., Krokhotin, A., Miller, E.L., Tang, Y., Panagiotakos, G., and Crabtree, G.R. (2021). BAF subunit switching regulates chromatin accessibility to control cell cycle exit in the developing mammalian cortex. Genes Dev. *35*, 335–353. https://doi.org/10.1101/gad.342345.120.

53. Jin, Y., Gao, X., Lu, M., Chen, G., Yang, X., Ren, N., Song, Y., Hou, C., Li, J., Liu, Q., et al. (2022). Loss of BAF (mSWI/SNF) chromatin-remodeling ATPase Brg1 causes multiple malformations of cortical development in mice. Hum. Mol. Genet. *31*, 3504–3520. https://doi.org/10.1093/hmg/ddac127.

54. Cueille, N., Blanc, C.T., Popa-Nita, S., Kasas, S., Catsicas, S., Dietler, G., and Riederer, B.M. (2007). Characterization of MAP1B heavy chain interaction with actin. Brain Res. Bull. *71*, 610–618. https://doi.org/10.1016/j.brainresbull.2006.12.003.

55. Mahmood, S.R., Xie, X., Hosny El Said, N., Venit, T., Gunsalus, K.C., and Percipalle, P. (2021). β-actin dependent chromatin remodeling mediates compartment level changes in 3D genome architecture. Nat. Commun. *12*, 5240. https://doi.org/10.1038/s41467-021-25596-2.

56. Chang, L., Jones, Y., Ellisman, M.H., Goldstein, L.S.B., and Karin, M. (2003). JNK1 Is Required for Maintenance of Neuronal Microtubules and Controls Phosphorylation of Microtubule-Associated Proteins. Dev. Cell *4*, 521–533. https://doi.org/10.1016/S1534-5807(03)00094-7.

57. Auburger, G., Gispert, S., Torres-Odio, S., Jendrach, M., Brehm, N., Canet-Pons, J., Key, J., and Sen, N.E. (2019). SerThr-PhosphoProteome of brain from aged PINK1-KO+A53T-SNCA mice reveals pT1928-MAP1B and pS3781-ANK2 deficits, as hub between autophagy and synapse changes. Int. J. Mol. Sci. *20*, 3284. https://doi.org/10.3390/ijms20133284.

58. Gong, C.X., and Iqbal, K. (2008). Hyperphosphorylation of Microtubule-Associated Protein Tau: A Promising Therapeutic Target for Alzheimer Disease. Curr. Med. Chem. *15*, 2321–2328. https://doi.org/10.2174/092986708785909111.

59. Matsumoto, S., Banine, F., Struve, J., Xing, R., Adams, C., Liu, Y., Metzger, D., Chambon, P., Rao, M.S., and Sherman, L.S. (2006). Brg1 is required for murine neural stem cell maintenance and gliogenesis. Dev. Biol. *289*, 372–383. https://doi.org/10.1016/j.ydbio.2005.10.044.

60. Ren, G., Ku, W.L., Ge, G., Hoffman, J.A., Kang, J.Y., Tang, Q., Cui, K., He, Y., Guan, Y., Gao, B., et al. (2024). Acute depletion of BRG1 reveals its primary function as an activator of transcription. Nat. Commun. *15*, 4561. https://doi.org/10.1038/s41467-024-48911-z.

61. Forero, A., Pipicelli, F., Moser, S., Baumann, N., Grätz, C., Gonzalez Pisfil, M., Pfaffl, M.W., Pütz, B., Kielkowski, P., Cernilogar, F.M., et al. (2024). Extracellular vesicle-mediated trafficking of molecular cues during human brain development. Cell Rep. *43*, 114755. https://doi.org/10.1016/j.celrep.2024.114755.

62. Yeyati, P.L., Schiller, R., Mali, G., Kasioulis, I., Kawamura, A., Adams, I.R., Playfoot, C., Gilbert, N., van Heyningen, V., Wills, J., et al. (2017). KDM3A coordinates actin dynamics with intraflagellar transport to regulate cilia stability. J. Cell Biol. *216*, 999–1013. https://doi.org/10.1083/jcb.201607032.

63. Donlin, L.T., Andresen, C., Just, S., Rudensky, E., Pappas, C.T., Kruger, M., Jacobs, E.Y., Unger, A., Zieseniss, A., Dobenecker, M.W., et al. (2012). Smyd2 controls cytoplasmic lysine methylation of Hsp90 and myofilament organization. Genes Dev. *26*, 114–119. https://doi.org/10.1101/gad.177758.111.

64. Abdollahi, M.R., Morrison, E., Sirey, T., Molnar, Z., Hayward, B.E., Carr, I.M., Springell, K., Woods, C.G., Ahmed, M., Hattingh, L., et al. (2009). Mutation of the Variant α-Tubulin TUBA8 Results in Polymicrogyria with Optic Nerve Hypoplasia. Am. J. Hum. Genet. *85*, 737–744. https://doi.org/10.1016/j.ajhg.2009.10.007.

65. McFadden, J.R., Tolete, C.D.P., Huang, Y., Macnamara, E., Sept, D., Nesterova, G., Gahl, W.A., Sackett, D.L., and Malicdan, M.C.V. (2023). Clinical, genetic, and structural characterization of a novel TUBB4B tubulinopathy. Mol. Genet. Metab. Rep. *36*, 100990. https://doi.org/10.1016/j.ymgmr.2023.100990.

66. Parrini, E., Ramazzotti, A., Dobyns, W.B., Mei, D., Moro, F., Veggiotti, P., Marini, C., Brilstra, E.H., Dalla Bernardina, B., Goodwin, L., et al. (2006). Periventricular heterotopia: Phenotypic heterogeneity and correlation with Filamin a mutations. Brain *129*, 1892–1906. https://doi.org/10.1093/brain/awl125.

67. Perez-Riverol, Y., Bandla, C., Kundu, D.J., Kamatchinathan, S., Bai, J., Hewapathirana, S., John, N.S., Prakash, A., Walzer, M., Wang, S., et al. (2025). The PRIDE database at 20 years: 2025 update. Nucleic Acids Res. *53*, D543–D553. https://doi.org/10.1093/nar/gkae1011.

68. Raudvere, U., Kolberg, L., Kuzmin, I., Arak, T., Adler, P., Peterson, H., and Vilo, J. (2019). G:Profiler: A web server for functional enrichment analysis and conversions of gene lists (2019 update). Nucleic Acids Res. *47*, W191–W198. https://doi.org/10.1093/nar/gkz369.

69. Supek, F., Bošnjak, M., Škunca, N., and Šmuc, T. (2011). Revigo summarizes and visualizes long lists of gene ontology terms. PLoS One *6*, e21800. https://doi.org/10.1371/journal.pone.0021800.

70. Wolf, F.A., Angerer, P., and Theis, F.J. (2018). SCANPY: Large-scale single-cell gene expression data analysis. Genome Biol. *19*, 15. https://doi.org/10.1186/s13059-017-1382-0.

71. Wolock, S.L., Lopez, R., and Klein, A.M. (2019). Scrublet: Computational Identification of Cell Doublets in Single-Cell Transcriptomic Data. Cell Syst. *8*, 281–291.e9. https://doi.org/10.1016/j.cels.2018.11.005.

72. Liu, A., Peng, B., Pankajam, A.V., Duong, T.E., Pryhuber, G., Scheuermann, R.H., and Zhang, Y. (2024). Discovery of optimal cell type classification marker genes from single cell RNA sequencing data. BMC Methods *1*, 15. https://doi.org/10.1186/s44330-024-00015-2.

73. Langmead, B., and Salzberg, S.L. (2012). Fast gapped-read alignment with Bowtie 2. Nat. Methods *9*, 357–359. https://doi.org/10.1038/nmeth.1923.

74. Zhang, Y., Liu, T., Meyer, C.A., Eeckhoute, J., Johnson, D.S., Bernstein, B.E., Nusbaum, C., Myers, R.M., Brown, M., Li, W., et al. (2008). Model-based analysis of ChIP-Seq (MACS). Genome Biol. *9*, R137. https://doi.org/10.1186/gb-2008-9-9-r137.

75. Ramírez, F., Ryan, D.P., Grüning, B., Bhardwaj, V., Kilpert, F., Richter, A.S., Heyne, S., Dündar, F., and Manke, T. (2016). deepTools2: a next generation web server for deep-sequencing data analysis. Nucleic Acids Res. *44*, W160–W165. https://doi.org/10.1093/nar/gkw257.

76. McLean, C.Y., Bristor, D., Hiller, M., Clarke, S.L., Schaar, B.T., Lowe, C.B., Wenger, A.M., and Bejerano, G. (2010). GREAT improves functional interpretation of cis-regulatory regions. Nat. Biotechnol. *28*, 495–501. https://doi.org/10.1038/nbt.1630.

77. Schnitzbauer, J., Strauss, M.T., Schlichthaerle, T., Schueder, F., and Jungmann, R. (2017). Super-resolution microscopy with DNA-PAINT. Nat. Protoc. *12*, 1198–1228. https://doi.org/10.1038/nprot.2017.024.

78. Borchin, B., Chen, J., and Barberi, T. (2013). Derivation and FACS-mediated purification of PAX3+/PAX7+ skeletal muscle precursors from human pluripotent stem cells. Stem Cell Rep. *1*, 620–631. https://doi.org/10.1016/j.stemcr.2013.10.007.

79. D'Amour, K.A., Agulnick, A.D., Eliazer, S., Kelly, O.G., Kroon, E., and Baetge, E.E. (2005). Efficient differentiation of human embryonic stem cells to definitive endoderm. Nat. Biotechnol. *23*, 1534–1541. https://doi.org/10.1038/nbt1163.

80. Shi, Y., Kirwan, P., and Livesey, F.J. (2012). Directed differentiation of human pluripotent stem cells to cerebral cortex neurons and neural networks. Nat. Protoc. *7*, 1836–1846. https://doi.org/10.1038/nprot.2012.116.

81. Lancaster, M.A., and Knoblich, J.A. (2014). Generation of cerebral organoids from human pluripotent stem cells. Nat. Protoc. *9*, 2329–2340. https://doi.org/10.1038/nprot.2014.158.

82. Giandomenico, S.L., Sutcliffe, M., and Lancaster, M.A. (2021). Generation and long-term culture of advanced cerebral organoids for studying later stages of neural development. Nat. Protoc. *16*, 579–602. https://doi.org/10.1038/s41596-020-00433-w.

83. Noble, M., Lewis, S.A., and Cowan, N.J. (1989). The Microtubule Binding Domain of Microtubule-Associated Protein MAP1B Contains a Repeated Sequence Motif Unrelated to That of MAP2 and Tau. J. Cell Biol. *109*, 3367–3376. https://doi.org/10.1083/jcb.109.6.3367.

84. Villarroel-Campos, D., and Gonzalez-Billault, C. (2014). The MAP1B case: An old MAP that is new again. Dev. Neurobiol. *74*, 953–971. https://doi.org/10.1002/dneu.22178.

85. Esgleas, M., Falk, S., Forné, I., Thiry, M., Najas, S., Zhang, S., Mas-Sanchez, A., Geerlof, A., Niessing, D., Wang, Z., et al. (2020). Trnp1 organizes diverse nuclear membrane-less compartments in neural stem cells. EMBO J. *39*, e103373. https://doi.org/10.15252/embj.2019103373.

86. Wiśniewski, J.R., Zougman, A., Nagaraj, N., and Mann, M. (2009). Universal sample preparation method for proteome analysis. Nat. Methods *6*, 359–362. https://doi.org/10.1038/nmeth.1322.

87. Grosche, A., Hauser, A., Lepper, M.F., Mayo, R., von Toerne, C., Merl-Pham, J., and Hauck, S.M. (2016). The proteome of native adult Müller glial cells from Murine retina. Mol. Cell. Proteomics *15*, 462–480. https://doi.org/10.1074/mcp.M115.052183.

88. Tyanova, S., and Cox, J. (2018). Perseus: A bioinformatics platform for integrative analysis of proteomics data in cancer research. Methods Mol. Biol. *1711*, 133–148. https://doi.org/10.1007/978-1-4939-7493-1_7.

89. Molitor, L., Klostermann, M., Bacher, S., Merl-Pham, J., Spranger, N., Burczyk, S., Ketteler, C., Rusha, E., Tews, D., Pertek, A., et al. (2023). Depletion of the RNA-binding protein PURA triggers changes in post-transcriptional gene regulation and loss of P-bodies. Nucleic Acids Res. *51*, 1297–1316. https://doi.org/10.1093/nar/gkac1237.

90. Käll, L., Canterbury, J.D., Weston, J., Noble, W.S., and MacCoss, M.J. (2007). Semi-supervised learning for peptide identification from shotgun proteomics datasets. Nat. Methods *4*, 923–925. https://doi.org/10.1038/nmeth1113.

91. Lepiemme, F., Silva, C.G., and Nguyen, L. (2021). Time lapse recording of cortical interneuron migration in mouse organotypic brain slices and explants. Star Protoc. *2*, 100467. https://doi.org/10.1016/j.xpro.2021.100467.

92. Heumos, L., Schaar, A.C., Lance, C., Litinetskaya, A., Drost, F., Zappia, L., Lücken, M.D., Strobl, D.C., Henao, J., Curion, F., et al. (2023). Best practices for single-cell analysis across modalities. Nat. Rev. Genet. *24*, 550–572. https://doi.org/10.1038/s41576-023-00586-w.

93. Dimitrov, D., Schäfer, P.S.L., Farr, E., Rodriguez-Mier, P., Lobentanzer, S., Badia-I-Mompel, P., Dugourd, A., Tanevski, J., Ramirez Flores, R.O., and Saez-Rodriguez, J. (2024). LIANA+ provides an all-in-one framework for cell–cell communication inference. Nat. Cell Biol. *26*, 1613–1622. https://doi.org/10.1038/s41556-024-01469-w.

94. Korsunsky, I., Millard, N., Fan, J., Slowikowski, K., Zhang, F., Wei, K., Baglaenko, Y., Brenner, M., Loh, P.R., and Raychaudhuri, S. (2019). Fast, sensitive and accurate integration of single-cell data with

Harmony. Nat. Methods *16*, 1289–1296. https://doi.org/10.1038/s41592-019-0619-0.

95. Galaxy Community (2024). The Galaxy platform for accessible, reproducible, and collaborative data analyses: 2024 update. Nucleic Acids Res. *52*, W83–W94. https://doi.org/10.1093/nar/gkae410.

96. Ge, S.X., Jung, D., and Yao, R. (2020). ShinyGO: a graphical gene-set enrichment tool for animals and plants. Bioinformatics *36*, 2628–2629. https://doi.org/10.1093/bioinformatics/btz931.

97. Strauss, S., and Jungmann, R. (2020). Up to 100-fold speed-up and multiplexing in optimized DNA-PAINT. Nat. Methods *17*, 789–791. https://doi.org/10.1038/s41592-020-0869-x.

98. Tokunaga, M., Imamoto, N., and Sakata-Sogawa, K. (2008). Highly inclined thin illumination enables clear single-molecule imaging in cells. Nat. Methods *5*, 159–161. https://doi.org/10.1038/nmeth1171.

99. Edelstein, A.D., Tsuchida, M.A., Amodaj, N., Pinkard, H., Vale, R.D., and Stuurman, N. (2014). Advanced methods of microscope control using μManager software. J. Biol. Methods *1*, e10. https://doi.org/10.14440/jbm.2014.36.

100. Ma, H., Chen, M., Nguyen, P., and Liu, Y. (2024). Toward drift-free high-throughput nanoscopy through adaptive intersection maximization. Sci. Adv. *10*, eadm7765. https://doi.org/10.1126/sciadv.adm7765.

101. Ester, M., Kriegel, H.-P., Sander, J., and Xu, X. (1996). A Density-Based Algorithm for Discovering Clusters in Large Spatial Databases with Noise. In KDD-96. Proceedings, pp. 226–231.

Please cite this article in press as: Merino et al., Nuclear proteome reveals microtubule-associated protein regulating fate and disease, Cell (2026), https://doi.org/10.1016/j.cell.2026.05.019

CellPress
OPEN ACCESS

STAR★METHODS

KEY RESOURCES TABLE

REAGENT or RESOURCE	SOURCE	IDENTIFIER
Antibodies		
Chick polyclonal anti-GFP	Aves Lab	Cat # GFP-1020; RRID: AB_10000240
Mouse IgG1 monoclonal [P3U1] anti-PAX6	DSHB / HMGU MAB	RRID: AB_528427
Rabbit polyclonal anti-MAP1B	Abcam	Cat # ab154333
Rabbit monoclonal [EPR19012] anti- TBR2	Abcam	Cat # ab183991; RRID: AB_2721040
Mouse IgG2b monoclonal [H-8] anti-MAP1B	Santa Cruz	Cat # sc-365668; RRID: AB_10847224
Rabbit polyclonal anti-RFP	Rockland/Biomol	Cat # 600-401-379; RRID: AB_2209751
Mouse IgG2b monoclonal [10H9.1] anti-SOX2	Merck/Millipore	Cat # MAB4423; RRID: AB_11205572
Mouse IgG1 monoclonal [M2] anti-Flag	Sigma-Aldrich	Cat # F3165; RRID: AB_259529
Mouse IgG1 monoclonal [6C5] anti-GAPDH	Santa Cruz	Cat # sc32233; RRID: AB_627679
Rabbit polyclonal anti-LAMIN B1	Abcam	Cat # ab16048; RRID: AB_443298
Mouse IgG1 monoclonal anti-ACTB	Santa Cruz	Cat # sc-47778; RRID: AB_626632
Rabbit polyclonal anti-PAX6	Biolegend	Cat # 901302; RRID: AB_2749901
Mouse IgG1 monoclonal [HM-2] anti-MAP2	Merck/Sigma-Aldrich	Cat # M4403; RRID: AB_477193
Mouse IgG1 monoclonal [SC-35] anti-SC35	Abcam	Cat # ab11826; RRID: AB_298608
Rabbit polyclonal anti-SRRM2	Abcam	Cat# ab122719; RRID: AB_11130779
Rabbit Polyclonal anti-SMARCC1	Invitrogen	Cat# PA5-30174; RRID: AB_2547648
Rabbit monoclonal [EPR25248-95] anti-KPNA2	Abcam	Cat # ab289858
Rabbit polyclonal anti-MTA2	Bethyl	Cat # A300-395A; RRID: AB_386106
Rabbit monoclonal [EPR25A] - Isotype Control	Abcam	Cat # ab172730; RRID: AB_2687931
Mouse IgG2b monoclonal [MG2b-57] - Isotype Control	Abcam	Cat # ab18428; RRID: AB_3694029
Rabbit monoclonal [EPNCIR111A] anti-BRG1	Abcam	Cat # ab110641; RRID: AB_10861578
Rabbit monoclonal [DA1E] – Isotype control	Cell Signalling	Cat # 66362; RRID: AB_2924329
Rabbit polyclonal anti-NEUROD2	Abcam	Cat # ab104430; RRID: AB_10975628
Rabbit monoclonal [71D10] anti-MYC	Cell Signaling	Cat # 2278; RRID: AB_490778
Mouse IgG1 monoclonal [TI10] anti-FLNA	Merck/Millipore	Cat # MAB1680; RRID: AB_94323
Mouse IgG1 monoclonal [Rat-401] anti-Nestin	Merck/Millipore	Cat # MAB353; RRID: AB_94911
Guinea pig polyclonal anti-SATB2	SYSY	Cat # 327 004; RRID: AB_2620070
Rat monoclonal [25B6] anti-CTIP2	Abcam	Cat # ab18465; RRID: AB_2064130
Guinea pig polyclonal anti-DCX	Merck/Millipore	Cat #AB2253; RRID: AB_1586992
Rat monoclonal anti-SOX2	ThermoFisher	Cat # 740013T; RRID: AB_3093719
Mouse IgG1 monoclonal [M2] anti-Flag	Sigma	Cat # F1804; RRID: AB_262044
Mouse IgG1 monoclonal [AC-15] anti-ACTB	Abcam	Cat # ab6276; RRID: AB_2223210
Mouse IgG1 monoclonal [13B10-1A10] anti-PAX6	ThermoFisher	Cat #MA1-109; RRID: AB_2536820
sdAb anti-rabbit IgG (DNA-PAINT)	Nanotag	Cat # N2405
sdAb anti-mouse Ig kappa light chain (DNA-PAINT)	Nanotag	Cat # N1205
Chemicals, peptides, and recombinant proteins		
Fast Green dye	Sigma-Aldrich	F7258
D(+)-Sucrose	Carl Roth	4621
Neg-50™ Frozen Section Medium	ThermoFisher	6502
Hank's Balanced Salt Solution (HBSS)	ThermoFisher	14025100
10 mM HEPES	Gibco	15630-056
DMEM + GlutaMAX™	Gibco	61965

(*Continued on next page*)

Please cite this article in press as: Merino et al., Nuclear proteome reveals microtubule-associated protein regulating fate and disease, Cell (2026), https://doi.org/10.1016/j.cell.2026.05.019

Continued

REAGENT or RESOURCE	SOURCE	IDENTIFIER
Fetal bovine serum (FBS)	PAN Biotech	P30-3302
Neurobasal Medium	Gibco	21103049
GlutaMAX™ Supplement	Gibco	35050038
N-2 supplement (N2)	Gibco	17502048
B-27 supplement (B27)	Gibco	17504044
Penicillin-Streptomycin (Pen/Strp)	Gibco	15140-122
MEM Non-Essential Amino Acids Solution (NEAA)	Gibco	11140-035
Sodium Pyruvate	Gibco	11360070
0.05% Trypsin	Gibco	25300
2-mercaptoethanol	Gibco	31350010
Insulin	Sigma-Aldrich	I9278
SB431642	StemCell Tech.	72232
Dorsomorphin	StemCell Tech.	72102
Rock inhibitor Y-27632 (2HCL)	StemCell Tech.	72304
Accutase (for iPSCs-derived NSCs)	Gibco	A1110501
Accutase (for cerebral organoids)	Sigma-Aldrich	A6964
DMEM/F12 GlutaMax	Gibco	31331-028
Matrigel	Corning	354234
Knock-out Serum Replacement	Gibco	10828-028
Human recombinant Fibroblast Growth Factor (FGF)	Life technologies	13256029
Insulin	Gibco	19278
DAPI	Sigma-Aldrich	D9542
Bovine Serum Albumin (BSA)	Sigma-Aldrich	A2153
poly-D-lysine	Sigma-Aldrich	P1149
Triton-X100	Carl Roth	3051
Aqua Polymount	Polyscience	18606-5
Benzonase® Nuclease	Millipore	E1014
Dynabeads™ Protein A	Invitrogen	10001D
Dynabeads™ Protein G	Invitrogen	10003D
Lipofectamine 2000	Invitrogen	11668019
Opti-MEM™ GlutaMAX™	Gibco	51985034
pluriStrainer Mini 40 μm	PluriSelect	43-10040-60
Pierce™ Protease and Phosphatase Inhibitor	ThermoFisher	A32959
cOmplete™, Mini Protease Inhibitor Cocktail	Roche	11697498001
2-Mercaptoethanol (for IPs)	Sigma-Aldrich	M3148
RIPA Buffer	Sigma-Aldrich	R0278
Pierce™ Lane Marker Reducing Sample Buffer	ThermoFisher	39000
Certified PCR Low Melt Agarose	Bio-rad	1613114
Immersion Oil W 2010	Zeiss	444969-0000-000
Dimethylsulfoxide (DMSO)	Sigma-Aldrich	D2438
Sodium chloride 5 M (DNA-PAINT)	ThermoFisher	AM9759
Ultrapure water (DNA-PAINT)	ThermoFisher	10977-035
Tris 1 M (DNA-PAINT)	ThermoFisher	AM9855G
EDTA 0.5 M (DNA-PAINT)	ThermoFisher	AM9260G
PBS 1X (DNA-PAINT)	ThermoFisher	20012-019
Salmon sperm DNA (DNA-PAINT)	ThermoFisher	15632011
Sodium azide (NaN_3)1% solution (DNA-PAINT)	G-Biosciences	786-750

(*Continued on next page*)

Please cite this article in press as: Merino et al., Nuclear proteome reveals microtubule-associated protein regulating fate and disease, Cell (2026), https://doi.org/10.1016/j.cell.2026.05.019

Continued

REAGENT or RESOURCE	SOURCE	IDENTIFIER
Triton X-100 (DNA-PAINT)	Carl Roth	6683.1
Tween 20 (DNA-PAINT)	Sigma-Aldrich	P9416-50ML
Glycerol (DNA-PAINT)	Sigma-Aldrich	65516-500ml
Methanol (DNA-PAINT)	Sigma-Aldrich	32213-2.5L
Protocatechuate 3,4-dioxygenase pseudomonas (PCD)	Sigma-Aldrich	P8279
3,4-dihydroxybenzoic acid (PCA)	Sigma-Aldrich	37580-25G-F
(+−)-6-hydroxy-2,5,7,8- tetra-methylchromane-2-carboxylic acid (Trolox)	Sigma-Aldrich	238813-5 G
Gold nanoparticles 90 nm diameter	Cytodiagnostics	G-90-100
Bifunctional maleimide-DBCO linker	Sigma-Aldrich	760668
Critical commercial assays		
EnGen® sgRNA Synthesis Kit, S. pyogenes	New England Biolabs	E3322
RNeasy Mini Kit	Qiagen	74104
Verso cDNA Systhesis Kit	Thermo Scientific	AB1453
EndoFree® Plasmid Maxi Kit	Qiagen	12362
Gateway™ LR Clonase™ II Enzyme mix	Invitrogen	11791020
Neural Tissue Dissociation Kit	Miltenyi Biotec	130-092-628
Red Blood Cell Lysis Solution (10×)	Miltenyi Biotec	130-094-183
Chromium Single Cell 3' (v3.1 Dual Index) kits	10x Genomics	1000262, 1000261, 1000269, 1000215, 1000127
DC Protein Assay	Bio-rad	500-0113, 500-0114, 500-0115,
ECL™ Western Blotting Detection Reagents	Sigma-Aldrich	GERPN2209
GeneArt™ Site-Directed Mutagenesis PLUS System	Invitrogen	A14604
Subcellular Protein Fractionation Kit for Tissues	ThermoFisher	87790
Cut&Run Assay Kit	Cell Signalling	86652
DNA Library Prep Kit for Illumina Systems	Cell Signalling	56795
Multiplex Oligos for Illumina Systems	Cell Signalling	46538
Deposited data		
NSCs subcellular fractionation and MAP1B interactome	This study	PRIDE: PXD063724
scRNAseq from *Map1b*-KD via IUE E13-E16	This study	BioStudies: S-BSST2574
BRG1 Cut&Run	This study	BioStudies: S-BSST2574
Experimental models: Cell lines		
HMGU1 induced pluripotent stem cells	CF-iPSC HMGU	ISFi001-A
N2A cells	ATCC	CCL-131
HMGU1 induced pluripotent stem cells_MAP1B WT	This study	WT
HMGU1 induced pluripotent stem cells_MAP1B c.3316C>T; p. R1106*	This study	MAP1B c.3316C>T
HMGU1 induced pluripotent stem cells_MAP1B c.2133delG; p. E712Kfs*10	This study	MAP1B c.2133delG
Experimental models: Organisms/strains		
C57BL/6J	Charles River	632C57BL/6J
Recombinant DNA		
Expression plasmid: pCAG-GFP-shControl	Dr. Adam O'Neill (gift)	shControl
Expression plasmid: pCAG-GFP-shMap1b	This study	shMap1b
Expression plasmid: pCAG-GFP-shMap1b#2	This study	shMap1b#2
Expression plasmid: p*Dcx*-GFP-shControl	This study	p*Dcx*_shControl

(*Continued on next page*)

Please cite this article in press as: Merino et al., Nuclear proteome reveals microtubule-associated protein regulating fate and disease, Cell (2026), https://doi.org/10.1016/j.cell.2026.05.019

Continued

REAGENT or RESOURCE	SOURCE	IDENTIFIER
Expression plasmid: p*Dcx*-GFP-shMap1b	This study	p*Dcx*_shMap1b
Expression plasmid: pCAG-ires-RFP	This study	RFP
Expression plasmid: pCAG-NESMap1b-ires-RFP	This study	NES-Map1b
Expression plasmid: pCAG-NLSMap1b-ires-RFP	This study	NLS-Map1b
Expression plasmid: pCAG-Flag-Map1b-ires-RFP	This study	MAP1B 1-2465
Expression plasmid: pCAG-Flag-Map1b(1-848)-ires-RFP	This study	MAP1B 1-848
Expression plasmid: pCAG-Flag-Map1b(524-848)-ires-RFP	This study	MAP1B 524-848
Expression plasmid: pCAG-Flag-Map1b(1-523)-ires-RFP	This study	MAP1B 1-523
Expression plasmid: pCAG-NLS-Flag-Map1b(1-523)-ires-RFP	This study	MAP1B 1-523
Expression plasmid: pCAG-NLS-Flag-Map1b(524-2465)-ires-RFP	This study	MAP1B 524-2465
Software and algorithms		
Spectronaut	Biognosis	19.9 software
Perseus	MaxQuant	2.0.11 software
Proteome Discoverer	Thermo Scientific	2.5 software
GeneProfiler	Raudvere et al.[68]	v1.0.0 software
REVIGO	Supek et al.[69]	v1.8.1 software
Cell Ranger	10x Genomics	version 3
ScanPy	Wolf et al.[70]	version 1.9.5
Scrublet	Wolock et al.[71]	version 0.2.3
FRmatch R package	Zhang et al.[43]	version 2.0.0
NSForest	Liu et al.[72]	version 3.9.2.5
scVelo	Bergen et al.[44]	version 0.2.5
CellRank	Lange et al.[45]	version 2.0.0.
Bowtie2	Langmead and Salzberg[73]	version 2.5.1
MACS	Zhang et al.[74]	version 3.0.1
DeepTools	Ramírez et al.[75]	version 3.5.4
GREAT	McLean et al.[76]	version 4.0.4
Affinity designer	Affinity	N/A
FACSDiva software	BD Biosciences	version 6.1.3
Prism	Graphpad	versions 8-10
Incucyte	Sartorius	https://www.sartorius.com/en
ImageJ/FIJI	ImageJ	https://imagej.net
Picasso	Schnitzbauer et al.[77]	https://github.com/jungmannlab/picasso

EXPERIMENTAL MODEL AND STUDY PARTICIPANT DETAILS

Experimental animals

C57BL/6J mice were kept in a 12 hour light-dark cycle with *ad libitum* access to water and food in the Core Facility Animal Models (CAM) of the Biomedical Center (Ludwig-Maximilians-Universität, Planegg-Martinsried). Mice (3-6 months age) were time-mated and the day of vaginal plug was considered as embryonic day 0 (E0). Both male and female embryos were used; sex was not determined at embryonic stages. All animal procedures were approved by the Government of Upper Bavaria (ROB) and performed in accordance with German animal welfare legislation (TierSchG) and GV-SOLAS (Society of Laboratory Animal Science).

Primary cerebral cortical cultures

Primary cerebral cortical cultures were derived from embryonic day 12 (E12) or E14 C57BL/6J mouse embryos (both male and female) as described in method details. Briefly, cerebral cortices were dissected and dissociated to obtain single-cell suspensions.

Please cite this article in press as: Merino et al., Nuclear proteome reveals microtubule-associated protein regulating fate and disease, Cell (2026), https://doi.org/10.1016/j.cell.2026.05.019

Cells were plated on poly-D-lysine-coated substrates and maintained under standard culture conditions at 37°C with 5% CO_2 in appropriate growth and differentiation media (see method details).

Neuro2A cells

Neuro2a (N2A) cells (ATCC, Cat#CCL-131) were cultured in 10% FBS, 1% Pen/Strep, 1% Sodium pyruvate, 1% Non-essential amino acids (NEAA) in DMEM + GlutaMax medium, at 37 °C with 5 % CO2. These were passaged by washing with 1X phosphate-buffered saline (PBS) and dissociation with 0.05 % Trypsin in a 1:10 ratio after reaching confluence. For testing the knockdown efficiency of *Map1b* shRNAs, N2A cells were collected 3 days after transfection and dissociated before being sorted and its proteins extracted (see method details).

Human induced pluripotent stem cells

Human induced pluripotent stem cells (iPSCs; HMGU1 line derived from male foreskin fibroblasts) were used as WT/control and to generate MAP1B mutant lines harboring the c.3316C>T (p.R1106*) and c.2133delG (p.E712Kfs*10) variants via CRISPR/Cas9-mediated genome editing. Heterozygous clones for each MAP1B cell line plus unedited control lines, which underwent the same procedure, were established and validated for genome editing, pluripotency, and differentiation capacity (see method details). Ethical approval was obtained in accordance with institutional guidelines.

iPSC-derived dorsal forebrain neural stem cells

Human iPSCs (HMGU1 background; unedited and edited) were differentiated into dorsal forebrain neural stem cells as previously described[7] (see method details) and harvested on day 15 for collection of neural stem cells.

Cerebral organoids

Cerebral organoids were generated from human iPSCs (HMGU1 background; unedited and edited) according to previously published protocols (see method details). Briefly, iPSCs were aggregated to form embryoid bodies, which were subsequently induced toward a neural fate and embedded in Matrigel to promote neuroepithelial tissue formation. Organoids were further matured in suspension culture under agitation to support tissue growth and organization. Organoids were maintained under standard culture conditions and collected at defined developmental stages for downstream analyses.

METHOD DETAILS

In utero electroporation (IUE)

IUEs were performed as licensed by the Government of Upper Bavaria (ROB) as described previously.[7] Briefly, at embryonic day 13 (E13), mice were anaesthetized by intraperitoneal injection of Fentanyl (0.05 mg/kg)/Midazolam (5 mg/kg)/Medetomidine (0.5 mg/kg). The shaved abdomen was opened by caesarean section to expose the uterus which was kept wet and warm by continuous application of pre-warmed saline solution. Endotoxin-free vectors were diluted to 0.7-1.3 μg/μl (keeping molar ratios constant, see details in table 'Recombinant DNA') in 0.9% NaCl and mixed with 0.01% Fast Green dye. 1 μl of the mix was injected into the lateral ventricle of the embryos by a self-made glass capillary of approx. 10 μm diameter. DNA was electroporated into the telencephalon with five pulses of 35 mV for 100 ms each, separated by 400ms intervals. The uterus was repositioned into the abdominal cavity and the abdominal wall was closed by surgical sutures. Anesthesia was antagonized by a subcutaneous injection of Buprenorphine (0.1 mg/kg)/Atipamezol (2.5 mg/kg/Flumazenil (0.5 mg/kg). Electroporated animals were collected at 2-, 3-, 5- or 16-days post electroporation (dpe).

Primary cortical cultures preparation

Embryos were placed in ice-cold Hank's Balanced Salt Solution (HBSS) supplemented with 10 mM HEPES. Both hemispheres were separated and enzymatically dissociated with 0.05% Trypsin for 6 minutes (E12) or 15 minutes (E14) at 37°C. The enzymatic activity was stopped by adding DMEM + GlutaMAX solution containing 10% Fetal bovine serum (FBS). A uniform single-cell mixture was achieved by mechanical dissociation using a Pasteur pipette. Cells were centrifuged for 5 minutes at 1000 rpm at 4°C and resuspended in DMEM + GlutaMAX containing 10% FBS and 1% Penicillin-Streptomycin (Pen/Strp) medium. Dissociated cells were seeded onto poly-D-lysine-coated (PDL) glass coverslips in 24-well plates at an approximately density of 400.000 cells/well or PDL-treated 8-well chambers (Ibidi, 80827) at an approximately density of 160.000-200.000 cells/well, and were cultured at 37°C with 5% CO2. The day after, differentiation medium consisting of 2% B27, 1% Pen/Strp in DMEM + GlutaMAX was added in a 1:1 ratio. Cells were washed and fixed after 1 or 3 days in vitro (DIV).

Generation of mutant iPSCs

Two PH-mutant iPSC lines harboring the MAP1B mutations c.3316C>T; p. R1106* and c.2133delG; p. E712Kfs*10 were generated by CRISPR/Cas9-mediated gene editing. For this, two locus-specific sgRNAs (sgRNA_C.2133DELG: 5'-ACCGCCAAAGGAA GTCAAGA-3' and sgRNA_C.3316C>T: 5'-CGAGGCCACCGCTTCTGATG-3') were produce from DNA oligo templates by in vitro transcription utilizing the EnGen® sgRNA Synthesis Kit, S. pyogenes, following manufacturer's instructions. As knock-in templates,

Please cite this article in press as: Merino et al., Nuclear proteome reveals microtubule-associated protein regulating fate and disease, Cell (2026), https://doi.org/10.1016/j.cell.2026.05.019

two specific targeting single stranded oligodeoxynucleotides (ssODNs, IDT; Coralville, USA) including the respective MAP1B mutations were used. In the case of MAP1B C.3316C>T, ONE additional silent mutation was introduced in the PAM motif to prevent re-targeting (ssODN_C.2133DELG: 5'CTTTGCGTCTTTAGGGAGCTTCTTAATTTCTTTTTTGGGTTCCTTTTCTT CCTTTTTCACTTCCTTCTTCTCTTCCTTCTTAACTTCTTCTTGACTTCCTTTGGCGGTGTTTCTTTCTTAACCTCTTTCTTGGGTTCT TTTTTCTCTTCTTTCTTGATCTCTTTTTTGACTTC -3' and ssODN_C.3316C>T: 5'-GTGGGCTCACTGGATATCTCAATAGTAGACT GAGTGTAGCCAGAGG TGGCAGTGAATTCCTCAGGCTGGTCTTCTCAATTCTCTTCATCAGAAGCGGTGGCCTCGCTCTCTGAGCCTCCAGGTAAAGTCT CATCATGAATTGAAGATGCAGGTTCTCGGC -3'). Human induced pluripotent stem cells (HMGU1) were passaged using Accutase (Sigma) for 10 min at 37°C, counted and electroporated as single cells using the 4D Nucleofector (Lonza Group Ltd) according to the manufacturer's instructions. For this, $1x10^6$ iPSCs, 15μg recombinant Cas9, 5.9μg and 10μg of the respective ssODN targeting oligo has been used. Subsequently, hiPSC colonies were clonalized and expanded for two rounds to ensure clonal origin. For characterization, genomic DNA was isolated using the Wizard Genomic DNA Purification Kit (Promega, Mannheim, Germany) following manufacturer's instructions. Correct knock-in of the respective mutations was verified by Sanger sequencing of amplicons covering the ssODN integration site. In total, heterozygous clones for each MAP1B cell line plus unedited control lines, which underwent the same procedure, have been selected.

Following the editing process, the PH-mutant iPSC clones were evaluated for their capacity to differentiate across three embryonic lineages. In summary, two consecutive passages were seeded as single cells in a 24-well plate with $2.5x10^5$ cells/well, achieving approximately 90% confluency. The remaining cells were collected for subsequent RNA extraction, which was used to normalize the differentiated samples. Two days following the initial seeding, the cells were differentiated for a period of five days using a self-made medium in accordance with published protocols.[78–80] To induce ectoderm commitment, the cells were transferred to a DMEM/F-12:Neurobasal mixture containing 1xN2, 1xB27-Vitamin A, and 4 μg/ml Insulin, along with 1 μM Dorsomorphin, 10 μM SB431542, and 10 ng/ml bFGF. For mesoderm commitment, the cells were switched to a DMEM/F12 medium, which was supplemented with 1xB27-Vitamin A and 10 μM CHIR 99021. For endoderm commitment, the cells were switched to DMEM/F12 supplemented with 1x B27, 1 μM CHIR 99021, 100 μg/ml Activin A, and 100 μM sodium butyrate. At the conclusion of the differentiation process, the cells were washed and collected in RLT buffer. The isolation of RNA was conducted in accordance with RNeasy Mini Kit, according to manufacturer's instructions. Reverse transcription was conducted using 500 ng of RNA as the input material, employing the Verso cDNA Synthesis Kit. The resulting cDNA was diluted 1:5. The complete reaction for the RT-qPCR contained 5 μl of SYBR Green Master Mix, 1 μl of cDNA, and 1 μl of each 10 μM forward and reverse primers topped off with nuclease free water for a total volume of 10 μl/reaction. The relative expression of the marker of interest was calculated using the Delta-Delta Ct method, which was normalized to GAPDH.

IPSC-derived dorsal forebrain neural stem cells differentiation

Induced pluripotent stem cells (HMGU1 background; unedited and edited) were differentiated into dorsal forebrain neural stem cell as previously described.[7] Briefly, cells were cultured in neural induction medium (N3) containing DMEM/F12 + GlutaMAX, N2, 5 μg/ml insulin, 1 mM L-glutamine, 100 μm non-essential amino acids, 100 μM 2-mercaptoethanol, 50 U/ml penicillin, 50 mg/ml streptomycin, Neurobasal medium and B27 with vitamin A, supplemented with 0.5 μM Dorsomorphin and 10 μM SB431542 for the first 10 days. On day 10, cells were dissociated into single cell suspensions via incubation with Accutase and replated on laminin-coated plates in a 1:3-1:4 ratio with N3 medium supplemented with 10 μM ROCK inhibitor.

Generation of cerebral organoids

Cerebral organoids were generated from iPSCs at ~80% confluence according to previously published protocols.[81,82] Briefly, cells were dissociated with Accutase (Sigma-Aldrich) and resuspended in low bFGF medium containing DMEM/F12 + GlutaMax, 20% knock-out serum replacement, 3% FBS (Life technologies), 1% NEAA, 0.1 mM 2-mercaptoethanol, 4ng/ml human recombinant Fibroblast growth factor (FGF) with 50 μM ROCK inhibitor. Live cells (2000 per well) were seeded into low attachment 96-well plates and embryoid bodies (EBs) were formed after 24 hours. At day 2, human recombinant FGF and ROCK inhibitor were removed from the medium. EBs were cultured for 5-6 days and then transfered to neural induction medium to promote neuroepithelial tissue formation with radially organised pseudostratified epithelium. Around day 12, EBs were embedded in Matrigel and further cultured. On day 18, the organoids were placed on an orbital shaker at 57 rpm, and on day 20 the Matrigel was carefully removed. The medium was then changed every 3-4 days to support the development of brain tissue.

Recombinant DNA cloning

Sequences for the shRNAs (see table 'shRNA sequences') were designed using the Block-iT™ RNAi Designer tool by Invitrogen, purchased from Metabion (Planegg, Germany) and cloned in the plasmid pENTRY-GW-grandestuffer_GFP, containing the cDNA of the emerald green fluorescent protein. shRNAs sequences were flanked by sequences from murine miR-155 for optimized processing of the engineered RNAi. The resulting plasmids (pEntry plasmids) were subcloned using the Gateway® clonase system into destination vectors either under a CAG promoter or under the murine *Dcx* promoter, according to the manufacturer's protocol.

Mouse *Map1b* cDNA was obtained from Addgene (gift from Phillip Gordon-Weeks (Addgene plasmid #44396; http://n2t.net/addgene:44396; RRID:Addgene_44396)) and modified using the GeneArt™ Site-Directed Mutagenesis kit to fit the NCBI reference

Please cite this article in press as: Merino et al., Nuclear proteome reveals microtubule-associated protein regulating fate and disease, Cell (2026), https://doi.org/10.1016/j.cell.2026.05.019

sequence NM_008634.2 and subcloned in an expression vector, after a CAG promoter and before an internal ribosome entry site (IRES) element followed by the cDNA of the red fluorescent protein mScarlet. Nuclear export signal (NES) and nuclear localization signal (NLS) sequences were subcloned in the 5' region of *Map1b* cDNA. NES sequence: ctgcctccactggaaagactgacactc. NLS sequence: cccaagaagaagagaaaggttgaggacggcgaggg-cccagccgctaagagagtgaaactggattccggagctgctcctgccgccaagaaaaagaaactcgac.

MAP1B truncation plasmids were subcloned from the full-length MAP1B vector mentioned above using the Gateway® Clonase system. A 3xFlag tag (sequence: gactacaaagaccatgacggtgattataaagatcatgacatcgattacaaggatgacgatgacaag) was introduced to allow the visualization of the truncated protein. The truncated isoforms were then recombined into destination vectors under a CAG promoter and followed by an IRES element and a red fluorescent protein. The truncation positions for assessing the roles of the actin-binding and microtubule-binding domains were selected based on previous studies.[54,83,84]

Breasi-CRISPR

Breasi-CRISPR was performed as previously described.[48] Briefly, RNP complexes *were in utero* electroporated into the mouse developing cortex at E13 to edit neural clonal lineages selectively. For tagging endogenous MAP1B, a MYC tagged was introduced in its N terminal region (crRNA: rArGrCrCrGrGrCrArGrGrArUrGrGrCrGrArCrCrGrGrUrUrUrUrArGrArGrCrUrArUr

GrCrU; ssODNs: C*T*GCCCGATGGCTCCGGTTCGGTGGCTTCCACCACCACGGTCGCCAGGTCC

TCTTCGGAGATCAGCTTCTGCTCCATCCTGCCGGCTCTGCTCAAGCCTGAGAGAAGTGTTC*C*T. For introducing and visualizing MAP1B E712Kfs*10 mutation, a MYC tag was introduced before the mutation (crRNA: rCrUrCrUrUrUrCrUrUrCrArCr CrUrCrCrUrUrCrUrGrUrUr

UrUrArGrArGrCrUrArUrGrCrU; ssODNs: G*G*AGCTGAAGAAAGAGGTGAAGAAGGAAACAC CCCTGAAGGATGCCAAGAAG GAGGAGCAGAAGCTGATCTCCGAAGAGGACCTGTAAGTGAAGAAAGAGGAGAAGAAAGAAGTTAAAAAGGAAGAGAAGGAACC C*A*A). Two days after electroporation (E15), brains were collected for analysis. To validate correct targeting, electroporated cortices were genotyped. Genomic DNA isolated from individual cortices was subjected to PCR analysis using one primer complementary to the MYC tag sequence and another complementary to the flanking *Map1b* sequence. To confirm the generation of a truncated protein upon CRISPR insertion, a Western blot for MYC was performed on Breasi-CRISPR samples and compared to the protein produced by overexpressing a plasmid encoding the same *MAP1B* variant transfected into N2A cells. Upon validation of proper targeting, brains were collected and fixed in 4% PFA for 2 hours for imaging analysis of electroporated cell distribution and subcellular protein localization. For quantification, two sections from each of at least four brains, obtained from a minimum of three IUEs, were analyzed.

Cell transfection

Primary cortical cultures and N2A cells were transfected using Lipofectamine 2000 according to the manufacturer's protocol. Briefly, a DNA-lipid solution was prepared by mixing 1-2 μl Lipofectamine 2000 with 1-3 μg DNA in 200 μl Opti-MEM GlutaMAX medium per 12 mm coverslips in 24-well plates, 5 μl Lipofectamine 2000 with 2.5 μg on DNA in 500 μl Opti-MEM GlutaMAX medium per well of 6-well plates or 0.5 μl Lipofectamine 2000 with 0.5 μg DNA in 200 μl Opti-MEM GlutaMAX medium per well of 8-well Ibidi chambers. The DNA-lipid solution was incubated for 20-30 minutes at room temperature. Cells were washed with PBS 1X before adding 50 ul, 100 ul 500 ul of Opti-MEM GlutaMAX medium per well of 8-well chamber, 24-well plates or 6-well plates, respectively. The DNA-lipid solution was added by drops on top of the cells. A 1:1 DNA molar ratio between treatments and between treatment and rescue plasmids was used (see table 'Recombinant DNA'). After incubation with DNA-lipid solution, cells were washed with PBS 1X and cultured with their normal culture medium (see above).

Immunostaining

Embryonic brains were fixed with 4% PFA in PBS 1X for 2 hr (E12), 4 hr (E16) or 6 hr (E18) at 4°C, or with 100% ice-cold Methanol for 20 minutes (E12 for MAP1B co-staining with nuclear speckles marker) at -20°C. Electroporated P10 pups were perfused with 4% PFA in PBS 1X, and post fixed in 4% PFA in PBS 1X overnight at 4°C. Cerebral organoids were fixed with 4% PFA in PBS 1X for 30 minutes at 4°C. After fixation, brains and organoids were incubated in 30% sucrose in PBS 1X at 4°C overnight before being embedded in Neg-50™ Frozen section medium and snap frozen in dry ice. 25 μm thick sections (coronal for mouse brains) were obtained via cryosectioning. Cell cultures were fixed with 4% PFA in PBS 1X for 10 minutes at RT or with 100% ice-cold Methanol for 10 minutes at -20°C for MAP1B co-staining with nuclear speckles marker and subcellular distribution analysis in the mutant iPSCs-derived NSCs.

For immunostaining, sections or cells were washed with PBS 1X twice for 10 minutes, permeabilized with 0.2% Triton-X100 in PBS 1X for 20 minutes and blocked for 1 hour at RT with blocking solution, containing 2% bovine serum albumin (BSA), 0.5% Triton-X100 in PBS 1X. Sections were incubated overnight in blocking solution and primary antibody (see Table S5), followed by washes with 0.2% Triton-X100 in PBS and staining with secondary antibodies diluted in blocking solution with 0.1 mg/ml DAPI (4′,6-Diamidino-2-phenylindole dihydrochloride) for 1-2 hours at RT. After final washes, coverslips or slides were mounted with mounting medium Aqua polymount.

For immunostaining of cerebral organoids, sections were washed with PBS 1X and incubated with 0.01 M tri-sodium citrate buffer (pH 6) for 1 minute at 720 Watt followed by 10 minutes at 120 Watt. After letting them cool down at RT for 20 minutes, half of the volume of Tri-sodium citrate buffer was replaced with water, and incubated for 10 minutes at RT. After two washes with PBS 1X for 10 minutes, slides were post-fixed with 4% PFA for 10 minutes and then washed twice with PBS 1X for 5 minutes at RT. Slices

Please cite this article in press as: Merino et al., Nuclear proteome reveals microtubule-associated protein regulating fate and disease, Cell (2026), https://doi.org/10.1016/j.cell.2026.05.019

were then permeabilized with 0.2% Triton X-100 PBS 1X for 5 minutes and blocked with 10% normal goat serum, 3% BSA in 0.1% Tween PBS 1X for at least 1 hour at RT. Sections were incubated overnight in blocking solution and primary antibody (see Table S5), followed by washes with 0.2% Triton-X100 in PBS and staining with secondary antibodies diluted in blocking solution with 0.1 mg/ml DAPI for 1-2 hours at RT. After final washes, slides were mounted with mounting medium Aqua polymount.

Protein extraction

Subcellular protein extraction from cells in culture was performed as described previously.[85] Briefly, cells were washed with PBS 1X and lysed with Tween20 lysis buffer (25 mM HEPES pH 8, 20 mM NaCl, 2 mM EDTA, 1 mM PMSF, 0.5% Tween20) supplemented with protease+phosphatase inhibitors cocktail 1X, in a 1:1 ratio with the cell pellet's volume. The cytosolic fraction (supernantant) was separated after 336 x g for 10 minutes at 4°C. The pellet containing the nuclei was washed with Tween 20 lysis buffer, resuspended using Tween20 lysis buffer supplemented with 500 mM NaCl and sonicated 10 times for 10 sec ON/30 sec OFF. After a 10.000 x g centrifugation, the supernatant containing the nuclear soluble proteins was collected. To recover nuclear insoluble proteins, the pellet was resuspended in Benzonase Buffer (20 mM Tris-HCl pH 8.4, 150 mM NaCl, 1 mM $MgCl_2$, 1 mM PMSF), supplemented with protease+phosphatase inhibitors cocktail 1X, containing 1 ul of Benzonase® nuclease and incubated at 37°C for one hour at 750 rpm. After a 10.000 x g centrifugation for 15 minutes at 4°C, the supernatant containing the nuclear insoluble proteins was collected. Both nuclear soluble and insoluble protein solutions were mixed for obtaining a unique solution containing all nuclear proteins. When subcellular fractionation was followed by co-immunoprecipitation (see below), the sodium chloride concentration in each sample was adjusted to ensure comparable pulldown efficiencies.

Subcellular protein extraction from tissue and organoids was obtained using Subcellular Protein Fractionation Kit for Tissues from ThermoFisher following manufacturer's instructions, supplemented with protease+phosphatase inhibitors cocktail 1X. Nuclear soluble and insoluble fractions were mixed to obtain a unique nuclear fraction.

To obtain whole cell proteins, cell pellets were lysed using RIPA buffer with protease/protease+phosphatase inhibitors cocktail 1X, in a 1:1 ratio with the cell pellet's volume by mechanical dissociation. The sample was incubated 30 minutes in ice and centrifuged at 13.000 x g and 4°C for 15 minutes, after which the supernatant containing the proteins was collected.

Protein concentration was quantified via DC™ Protein Assay.

Immunoprecipitation

To detect most MAP1B interactions, we performed immunoprecipitation under low stringency conditions. For mass spectrometry-based interaction detection, 0.5 mg of cytosolic or nuclear-enriched proteins were diluted in 1 ml of lysis buffer (25 mM HEPES, pH 8.0; 2 mM EDTA; 1 mM PMSF; 0.5% Tween-20), supplemented with protease inhibitors/protease+phosphatase inhibitors, with a final NaCl concentration adjusted to 200 mM. All human iPSC-derived differentiations used for the MAP1B interactome were the same as those used for the subcellular proteome and therefore served as input samples.

For the validation of MAP1B interactors via Western blot analysis, 1 mg of nuclear enriched proteins were diluted in 1 ml of Lysis buffer containing 250/300 mM NaCl, except for the nuclear-enriched protein sample derived from E12 mouse cortex due to the unknown NaCl concentration in the solutions from ThermoFisher's subcellular fractionation kit (see above). For studying which MAP1B fragment interacts with BRG1, 2 mg of protein coming from transfected N2A cells was extracted using RIPA 1X with protease+phosphatase inhibitors.

Protein lysates were incubated with 2 μg of antibody (see Table S5) for 1 hour at 4°C on a rotator. After Dynabeads washing (1:1 Protein A:G), these were added 1:50 in each sample, and the mixture was incubated for 2 hours at 4°C on a rotator. After incubation, beads were retrieved and washed three times with 1 ml of IP washing buffer (25 mM HEPES pH 8.0, 2 mM EDTA, 200/300 mM NaCl, 1 mM PMSF, 0.5% Tween-20 supplemented with protease inhibitors and, when necessary, with phosphatase inhibitors) per sample for 15 minutes under rotation. The beads were further washed twice with IP base buffer (without Tween-20). For protein elution, 25 μl of 1X Laemmli buffer (32.9 mM Tris-HCl pH 6.8, 1% SDS, 2.5% 2-Mercaptoethanol) was added per sample, and the samples were boiled at 95°C for 10 minutes. The beads were removed, and the supernatant containing the eluted proteins was collected and stored at -80°C until further processing.

Mass spectrometry

The subcellular fractionation and interactome were all digested using a modified FASP procedure as described.[86,87]

For NSC's subcellular protomics analysis, digested peptides of the cellular fractionation samples were measured on a TimsTOF HT mass spectrometer (Bruker) equipped with a CaptiveSpray 2 source online coupled to a Vanquish Neo HPLC (Thermo Scientific). A nano-trap column was used (300-μm inner diameter (ID) × 5 mm, packed with Acclaim PepMap100 C18, 5μm, 100 Å from LC Packings) before separation by reversed-phase chromatography (Aurora 75μm ID × 250 mm, 1.8μm from Ionoptics) at 40°C. Peptides were eluted from the column at 250 nl/min using a nonlinear 45 min acetonitrile gradient from 3 to 40% in 0.1% formic acid. The DIA-Pasef method covered a mass range from 300 to 1,250 m/z and a mobility range from 0.65 to 1.35 1/ko, with a ramp and accumulation time of each 100ms. Precursor peptides were isolated using 34 variable MS/MS windows and 17 MS/MS ramps, resulting in a cycle time of 1.91 sec. Collision energy for 0.6 1/ko was set to 20 and for 1.6 1/ko to 59.

Generated measurement files were quantitatively analyzed in the Spectronaut 19.9 software (Biognosis) in directDIA using BGS settings, allowing for quantification on only proteotypic peptides and applying the QUANT2.0 label-free quantification method

allowing for a mean TOP3 protein group quantity calculation. Searches were performed using the Swissprot Human (20432 sequences) or Swissprot Mouse (17061 sequences) databases.

TOP3 protein group quantities were imported in Perseus 2.0.11 software[88] (MPI Martinsried). Abundances were log2 transformed and the data was filtered for at least 3 valid values per protein in at least one sample group per dataset. Missing values were imputed from normal distribution using default settings. The average quantities per protein per group were calculated and used for ratio calculations. Groups were compared applying a Student's t-test with (q) and without (p) Benjamini-Hochberg correction.

Enriched proteins in each subcellular fraction were considered as those with an adjusted p-value<0.05, and a logFoldChange>2. For specific protein subsets of interest, gene-set enrichment analysis (GSEA) was conducted using the *profile* function in GeneProfiler (v1.0.0), using the whole human or whole murine proteome as background, for human and mouse samples respectively. GSEA p-values were corrected for multiple testing using the Benjamini-Hochberg FDR method. Moreover, significant GO terms (adjusted p-value<0.05) were grouped for better interpretation using the REVIGO[69] tool (v1.8.1) with a cutoff of 0.4 and otherwise default parameters.

For MAP1B's interactome, digested peptides were measured on a QExactive HF X mass spectrometer (Thermo Scientific) online coupled to an Ultimate 3000 nano-RSLC (Thermo Scientific) as described.[89] Samples were automatically loaded onto the C18 precolumn cartridge and after 5 min eluted and separated on the C18 analytical column (nanoEase MZ HSS T3, 100 Å, 1,8 µm, 75 µm x 250 mm; Waters) in a 95 min non-linear acetonitrile gradient from 5 to 40% at a flow rate of 250 nl/min. MS spectra were recorded at a resolution of 60,000 with an automatic gain control (AGC) target of 3e6 and a maximum injection time of 30 ms from 300 to 1500 m/z. From the MS scan, the 15 most abundant peptide ions were selected for fragmentation via HCD with a normalized collision energy of 28, an isolation window of 1.6 m/z, and a dynamic exclusion of 30 s. MS/MS spectra were recorded at a resolution of 15,000 with an AGC target of 1e5 and a maximum injection time of 50 ms. Unassigned charges and charges of +1 and > +8 were excluded from precursor selection.

Generated raw files were quantitatively analyzed in the Proteome Discoverer 2.5 software (Thermo Scientific) for peptide and protein identification and quantification. Database search was performed using the Sequest HT search engine against the Swissprot Human database (20432 sequences, version 2020_02), considering full tryptic specificity, allowing for up to one missed cleavage, a precursor mass tolerance of 10 ppm and a fragment mass tolerance of 0.02 Da. Carbamidomethylation of cysteine was set as a static modification and deamidation of asparagine and glutamine, oxidation of methionine, and a combination of methionine loss with acetylation on protein N-terminus were allowed as dynamic modifications as well as phosphorylation of serine, threonine or tryptophane. The Percolator algorithm[90] was used for validating peptide spectrum matches. Match-between runs for label-free quantification was performed in the Minora node with limitations to a retention time window of 1 minute and a mass shift of 0.5 ppm. Quantification of proteins was based on peptide intensities for the TOP3 unique peptides per protein with a XCorr score >1 and a peptide FDR < 1% without normalization. Resulting raw protein abundances were filtered for a protein FDR of 1% and exported for further analysis in Perseus 2.0.11 software[88] (MPI Martinsried). Data was filtered for 3 valid values in the dataset, followed by log2 transformation of abundance values and low abundance imputation of missing values from normal distribution separately per column using default settings. The average abundances per group were used for calculation of IP enrichment values. All reported statistical tests correspond to Student's t-tests with Benjamini-Hochberg FDR corrections for multiple testing. Enriched interactors were considered as those with an adjusted p-value<0.05, and a logFoldChange>3. Enriched interactions are reported separately for cytosolic and nuclear-enriched fractions.

For proteins enriched in both fractions separately, gene-set enrichment analysis (GSEA) was conducted using the get_enrichment function in STRINGdb, using the whole human proteome as background. GSEA p-values were corrected for multiple testing using the Benjamini-Hochberg FDR method. Proteins with an adjusted p-value<0.05 were kept for further use. For GSEA-significant gene ontology term of interest, STRING networks including enriched peptides for each fraction were obtained and colored with the reported logFoldChange from fraction enrichment.

For MAP1B, both unphosphorylated and phosphorylated peptides were identified, and their respective abundance values across individual samples were exported for further analysis. To visualize peptide coverage along the MAP1B sequence, the start and end positions of all detected peptides were mapped onto an array corresponding to the length of the canonical MAP1B sequence. This approach allowed us to pinpoint areas of high or low peptide representation across the protein. To account for variability in sample coverage, peptide abundance values were normalized by the total peptide count per sample, ensuring comparability across samples regardless of total coverage. Additionally, to facilitate more direct comparisons of peptide abundance across samples, each peptide's abundance was scaled relative to its maximum value observed across samples, highlighting relative abundance variations within each peptide profile.

Western blot

After protein extraction and concentration determination (see above), protein solution was mixed with a reducing sample buffer in a 2X final concentration and boiled for 5 minutes at 95°C. Electrophoretic separation was conducted using polyacrylamide SDS gels with concentrations ranging from 6% to 12% and proteins were then transferred to nitrocellulose membrane. For immunodetection, membranes were blocked with 5% nonfat dry milk in TBS-T buffer (0.1% Tween 20 Tris-buffered saline, pH 7.4) for 1 hour and were incubated with primary antibodies diluted in 1% nonfat dry milk and TBS-T buffer overnight at 4°C. On the subsequent day, the membranes were incubated with horseradish peroxidase-conjugated secondary antibodies, diluted in blocking solution. Signal

was visualized by ECL method. Western blot images may originate from different membranes, involve different exposure times, or be obtained with or without prior stripping and therefore comparisons between different images should account for these variables.

Live imaging

For assessing cell death in cellular cultures, E12 cortical cells were prepared and transfected as described above. Two days post transfection, cultures were moved to a microscope equipped with a 37°C with 5% CO2 chamber (Leica DMi8 or Incucyte SX1 from Sartorius) and cells were imaged with an air 20X long-working distance objective for a total of 30 hours every 15-30 minutes.

Live imaging of organotypic slices was performed as described previously.[91] Briefly, 40-42 hours after *in utero* electroporation at E13, embryonic brains were dissected in ice-cold HBSS 1X and embedded in a 4% low-melting agarose solution, prepared the day before and kept at 37°C until used. Organotypic slices were cut using a vibratome (Leica VT 1200S) in ice-cold HBSS 1X, with a section thickness of 300 μm and transferred to a nylon filter (Millicell) in a glass-bottom Petri dish (MatTek) with Neurobasal medium supplemented with 2% B27, 1% N2, 1% GlutaMAX and 1% Pen/Strp. Organotypic slices were kept in an incubator at 37°C with 5% CO2 for 4 hours until placed in humidified stage-top incubator (Tokai Hit) at 37°C with 5% CO2 in a confocal microscope (FV1000, Olympus). Ten images located in the slice's center were acquired with Z-steps of 1.5 μm every 15 minutes for approx. 16 hours using a 40X long-working distance objective (LUMPlanFl NA0.8, Olympus) immersed in oil with water's refraction index (Zeiss).

Fluorescence-activated cell sorting (FACS)

For single-cell transcriptomic experiments, multiplexed cells (see above) were sorted in a common collecting tube, after filtering through a 40 μm cell strainer, using a BD FACSARIA III cell sorter (BD Biosciences). 10000-50000 events were sorted per treatment in each biological condition. The gating for GFP fluorescence was done using non-electroporated E16 cortices. We noticed that the number of cells with two oligo labels (as opposed to single-labeled cells) decreased to half (approx.) when the collecting tube was at 4°C during the FACS procedure.

For testing the knockdown efficiency of *Map1b* shRNAs in N2A were resuspended with either 0.05 % Trypsin and filtered through a 40 μm cell strainer. GFP+ (transfected) cells were sorted using a BD FACSARIA III cell sorter (BD Biosciences). Gates were set using cells coming from an untransfected well.

Single-cell transcriptomics

To perform single-cell transcriptomic analysis of the electroporated cortical cells, cerebral cortices were collected 3 dpe (E16) and dissociated using the Neural tissue dissociation kit (Miltenyi Biotec), before incubation with a red blood cell lysis solution (Miltenyi Biotec), both according to the manufacturer's protocol. Two to three separate pregnant females were used per experiment, each containing two to four electroporated embryos per treatment. Single cells were resuspended in 0.04% BSA in PBS 1X solution and each treatment per mother was multiplexed using the Cell multiplexing oligo labelling from 10x Genomics, according to manufacturer's protocol. GFP+ cells were sorted (see above), resuspended in 10% FBS in DMEM GlutaMAX medium and processed using the Single-Cell 3' Reagent Kits v3.1 from 10xGenomics, according to the manufacturer's protocol. Briefly, single cell gel beads in emulsion (GEMs) were generated and barcoded cDNA from poly-adenylated mRNA was purified and amplified for library construction. Samples were sequenced on a NovaSeq6000 at the Genomics Core Facility of the Helmholtz Center Munich.

Transcriptome alignment was performed against the Mouse genome (GRCm38), with the sequence of the multiplexing barcodes and reporter (GFP) included, using Cell Ranger v3. Quality control (QC) was performed following published best practices,[92] using ScanPy (version 1.9.5). In summary, for the dataset of electroporated cells under the pCAG promoter (pCAGd), cells containing at least 1000 genes and 2000 counts and a maximium of 10000 genes and 60000 counts were selected. Only cells containing a minimum of 0.0025 and a maximum 0.1 of mitochondrial count fraction were retained. In addition, genes expressed in less than 20 cells were removed. For the dataset from electroporated cells under the p*Dcx* promoter (pDCXd), given the deeper sequencing obtained, cells containing at least 2500 genes and 6000 counts and a maximium of 10000 genes and 60000 counts were selected. As with pCAGd, only cells containing a minimum of 0.0025 and a maximum 0.1 of mitochondrial count fraction were retained, and genes expressed in less than 20 cells were removed.

For both datasets, demultiplexing of the samples was carried out in a two-step process. First, initial thresholds for the expression of individual barcodes were defined as the local minimum of the bimodal marker expression distribution across cells. The selected resulting assignments were then treated as hard labels for a K nearest neighbors classifier, with K set to 150. All cells annotated with over 75% confidence (with at least 75% of neighbors assigned to the same label) were kept for further processing. Doublets were then removed using Scrublet[71] (version 0.2.3) individually for each sample, with a simulated doublet ratio of 3, and 50 principal components. Following established practices, all other parameters were left with their default values.

For each dataset individually, transcriptomic profiles were clustered using the Leiden community detection algorithm on a K nearest neighbor graph obtained using the 4000 most variable genes across cells. The resolution for each clustering solution was fine tuned in an iterative process, by maximizing the purity of the obtained clusters as defined by the expression of predefined cell type marker genes and identification of novel subpopulations. This resulted in resolution values of 0.6 and 0.9 for pCAGd and pDCXd, respectively. Differential gene expression was tested both between treatment and control cells per cluster individually, and between all cells on each cluster and the rest or specific subsets, using a Wilcoxon rank-sum test. P-values were adjusted for multiple testing with the Benjamini-Hochberg method on the false discovery rate. Genes with a p-value(adjusted)<0,05 and an

absolute fold-change>1.25 were considered significant. In the pDCX dataset, one of the three litters was removed from the analysis to avoid overestimation of the effects studied given its low *Map1b* KD levels (yet present in the raw data associated to this manuscript). In addition, cluster specific expression signatures were obtained using an additive Z-score over all genes differentially expressed against all other clusters, with an adjusted p-value lower than 0.05, and an effect size of at least 1 standard deviation. Clusters obtained on each dataset individually were matched using the FR match R package[43] (version 2.0.0). The minimal set of cell type markers was automatically obtained using the NSForest software (version 3.9.2.5).

Finally, cellular differentiation dynamics were studied in pCAGd using scVelo[44] (version 0.2.5). First, log-transformed counts of the 4000 most variable genes, as well as their spliced/unspliced transcript ratios, were used to compute a dynamical model of RNA velocity taking differential kinetics per cell type into account. The velocity model was then used to infer the latent differentiation time for both control and *Map1b*-KD cells. Moreover, a coarse differentiation state transition matrix was estimated using the estimated velocity vectors with software CellRank[45] (version 2.0.0, default parameters). Initial and terminal differentiation states were computed for both controls and *Map1b*-KD separately. Fate probabilities were then calculated for all terminal states, and a signature Z-score was constructed with those genes deemed as significant lineage drivers for the Neurons_unknown cluster.

To investigate whether the *Map1b*-KD affects cell-cell communication in the developing mouse cortex, we performed ligand-receptor interaction analysis using LIANA+.[93] We integrated our pCAGd scRNA-seq data with a reference dataset from the developing mouse cerebral cortex,[29] selecting only the E16 timepoint to match the developmental stage of our samples. Cell types with fewer than 200 cells for each condition from our dataset were excluded to ensure statistical robustness. Low-quality cells, doublets, and unassigned cells were removed from both datasets. After batch correction using Harmony[94] with 100 principal components, we ran LIANA's rank_aggregate method with the mouse consensus ligand-receptor resource separately for our Control and Map1b-KD conditions, each integrated with the reference background. Interactions were considered significant if both specificity_rank and magnitude_rank were $\leq$0.1. To compare interaction profiles between conditions, we applied Fisher's exact test to each source-target pair, testing whether the proportion of significant ligand-receptor pairs differed between Control and *Map1b*-KD. We intentionally did not apply multiple testing correction; if even this lenient approach fails to detect significant differences beyond what is expected by chance (~5%), this provides stronger evidence that *Map1b* knockdown does not substantially alter the cell-cell interaction landscape.

Cut and Run

Human iPSC-derived organoids were collected at Day 20 and a single-cell suspension was generated using the Neural tissue dissociation kit (Miltenyi Biotec), according to the manufacturer's protocol, while human iPSCs-derived NSCs were collected using Accutase. 300.000 non-fixed cells were counted for each reaction of Cut&Run, which was performed using Cut&Run assay kit (Cell Signaling Technologies) according to the manufacturer's instructions. Briefly, collected cells were incubated with Concanavalin A Magnetic beads, permeabilized and incubated with primary antibody against BRG1 (see Table S5) overnight at 4°C. A rabbit Isotype control antibody was used as IgG control (see Table S5). Subsequently, cells were incubated with pAG-MNase for 1 hour at 4°C. pAG-MNase was activated by adding calcium chloride and incubation at 4°C for 30 minutes. DNA was purified using phenol/chloroform extraction and ethanol precipitation as described in the manufacturer's protocol.

Cut&Run libraries were generated using the DNA Library Prep Kit for Illumina (Cell Signaling Technologies) and Multiplex Oligos for Illumina (Dual Index Primers, Cell Signaling Technologies) following the manufacturer's instructions, specifically for Cut&Run Assay kit protocol. Briefly, 3–5 ng of DNA was used for Cut&Run and IgG control samples, keeping the amount of DNA consistent between samples within each experiment. DNA ends were ligated with adaptors and amplified using PCR and dual Index primers. All clean-up steps were performed with 1.1× volume of SPRIselect® beads to increase the capture of smaller DNA fragments. Generated libraries were pooled and sequenced using 2 × 60 bp paired-end sequencing strategy on an Illumina® NextSeq1000 sequencer, at the depth of approx. 5 million reads per sample.

Sequenced reads were aligned to the human GRCh38 (hg38) genome using Bowtie2.[73] Peak calling was performed using the MACS3 pipeline[74] with corresponding IgG control bam files, using q value 0.02, and minimal fragment length 100. For human iPSCs-derived NSCs, two replicates were called peaks individually and only reproducible peaks between the replicates are considered for downstream analysis. An enrichment heatmap of the peaks was produced using deepTools's computeMatrix function[75] on Galaxy platform.[95] For human iPSCs-derived NSCs, merged bigwig files between replicates were generated using deepTools's bigwigCompare function[75] on Galaxy platform.[95] Called peaks were annotated using GREAT[76] for single nearest gene within proximal distance of 5kb upstream and 1kb downstream, plus distal distance up to 250kb. From annotated genes, GO term enrichment analysis was conducted using ShinyGO 0.85.[96]

DNA-paint

For MAP1B, BRG1 and ACTB DNA-PAINT in E12 cortical cultures, firstly the following buffers were prepared: Buffer C+ consisting of 1× PBS, 0.1 mM EDTA, 500 mM NaCl, and 0.05% Tween-20 (pH 7.4). Buffer C wash containing 1× PBS, 0.1 mM EDTA, and 500 mM NaCl (pH 7.4). Antibody incubation buffer consisting of 1× PBS supplemented with 1 mM EDTA, 0.02% Tween-20, 0.05% NaN_3, 2% BSA, and 0.05 mg/mL sheared salmon sperm DNA. A 100× Trolox stock solution was prepared by dissolving 100 mg Trolox in 430 µL 100% methanol, 345 µL 1 M NaOH, and 3.2 mL H_2O. A 40× PCA stock solution was prepared by dissolving

Please cite this article in press as: Merino et al., Nuclear proteome reveals microtubule-associated protein regulating fate and disease, Cell (2026), https://doi.org/10.1016/j.cell.2026.05.019

154 mg PCA in 10 mL H_2O, adjusting the pH to 9.0 with NaOH. A 100× PCD stock solution was prepared by dissolving 9.3 mg PCD in 13.3 mL buffer containing 100 mM Tris-HCl (pH 8), 50 mM KCl, 1 mM EDTA, and 50% glycerol. See key resources table for catalogue numbers.

Nanobody-DNA conjugation

Single-domain antibodies (sdAbs) against rabbit IgG and mouse Ig kappa light chain, carrying a single ectopic cysteine at the C-terminus, were used for site-specific conjugation. Conjugation to DNA-PAINT docking strands (see table 'Docking site sequences') was performed as previously described.[97] Briefly, the buffer was exchanged to 1× PBS supplemented with 5 mM EDTA (pH 7.0) using Amicon centrifugal filters (10 kDa MWCO). Free cysteines were reacted with a 20-fold molar excess of bifunctional maleimide-DBCO linker for 2–3 h on ice. Excess linker was removed by buffer exchange to PBS using Amicon centrifugal filters. Azide-functionalized DNA was added with 3–5 molar excess to the DBCO-nanobody and reacted overnight at 4°C. Unconjugated nanobody and free azide-DNA were removed by anion exchange using an ÄKTA Pure liquid chromatography system equipped with a Resource Q 1 ml column. Nanobody-DNA concentration was adjusted to 5 μM (in 1× PBS, 50% glycerol, 0.05% NaN3) and stored at −20°C.

DNA-PAINT microscopy setup

Fluorescence imaging was performed on a custom-built inverted microscope (Eclipse Ti2, Nikon Instruments) equipped with a Perfect Focus System and configured for objective-type TIRF illumination. An oil-immersion objective (Apo SR HP TIRF 100×, NA 1.49, Nikon Instruments) was used. Excitation was provided by a 561 nm laser (1 W, MPB Communications) coupled through a manual TIRF module. The laser beam is passed through a cleanup filter (Chroma Technology, ZET561/10× for 560 nm excitation) and coupled into the microscope objective using a beam splitter (Chroma Technology, ZT561rdc). Fluorescence light is spectrally filtered with an emission filter (Chroma Technology, ET600/50m, and ET575lp) and imaged on an sCMOS camera (Hamamatsu Fusion BT) without further magnification, resulting in an effective pixel size of 130 nm after 2×2 binning, leading to an imaging field of view of approximately 67x67 μm^2. Highly Inclined and Laminated Optical (HILO)[98] illumination was used for all measurements. For imaging a central region of interest of 1,152 × 1,152 pixels (576 × 576 after binning) of the camera were chosen. 3D imaging was performed using a cylindrical lens (Nikon Instruments, N-STORM) in the detection path. The camera readout sensitivity is set to 16-bit and the readout bandwidth to 200 MHz. The scan mode of the camera was set to "ultra quiet scan" (readout noise = 0.7 e- r.m.s., 80 μs readout time per line). Image acquisition and microscope control is performed using μManager (Version 2.0.1).[99]

DNA-PAINT imaging

Cells were seeded on PDL-treated 8-well chambers (Ibidi, 80827) and after three days in culture they were fixed 4% PFA for 15 min and washed three times with 1× PBS. Samples were permeabilized with 0.25% Triton X-100 in antibody incubation buffer for 60 min at room temperature and washed three times with PBS. Samples were incubated with a 1:2 mixture of 90 nm gold nanoparticles in 1× PBS for 5 min at room temperature, followed by four washes with PBS. Primary antibodies against PAX6 (ThermoFisher) and BRG1 (Abcam) were applied in antibody incubation buffer and incubated overnight at 4°C (see table 'Experimental parameters for DNA-PAINT imaging'). In parallel, MAP1B (Santa cruz) and ACTB (Abcam) antibodies were preincubated with their respective secondary nanobodies as described in table 'Experimental parameters for DNA-PAINT imaging'.

The following day, samples were washed four times with PBS and incubated with secondary antibodies for 1 h at room temperature under gentle shaking. After washing, preincubated primary antibody–secondary nanobody complexes were pooled and applied to the samples for 60 min. Samples were washed extensively with PBS and buffer C wash, followed by incubation with DAPI (100 ng/mL) for 5 min.

Imaging was performed sequentially in buffer C+ using imager solutions. Knockdown and control cells were identified using 488 nm excitation, and PAX6-positive cells were identified using 640 nm excitation. Anti-mouse 647 secondary antibody signal was bleached prior to imaging. Targets were imaged using the 560 nm laser line at 90 W/cm^2 in HILO mode, acquiring 30,000 frames with 100 ms exposure time. Between imaging rounds, samples were washed with buffer C wash until no residual signal was detected.

Single-molecule localization analysis

Raw fluorescence data were reconstructed using the Picasso software package[77] (the latest version is available at https://github.com/jungmannlab/picasso). Drift correction was performed using the AIM algorithm[100] with gold nanoparticles as fiducial markers for all experiments. Channel alignment was carried out by cross-correlation of the fiducial gold nanoparticles using Picasso. For further analysis, localizations were restricted to a 260 nm-thick axial (z) region.

Clusters of nuclear proteins were identified using the DBSCAN algorithm.[101] The minimum number of localizations and the clustering radius were selected based on the imaging parameters of each individual super-resolution channel. To define a minimum localization threshold, background regions were analyzed and used as a baseline. Both DBSCAN parameters were further adjusted through visual inspection to determine cutoff values that distinguish background noise from specific protein clusters.

To quantitatively assess proximity of β-actin and MAP1B, first nearest-neighbor distance (NND) analysis was performed. Briefly, distances between each cluster in the target channel and the closest localization in the source channel were calculated for each cell using a k-nearest neighbors' algorithm. The resulting distance distributions were compared to complete spatial randomness (CSR) simulations generated using the same localization densities as observed in the experimental data. To account for differences in protein expression levels across cells and conditions, distance distributions (d_observed) were normalized to a

Please cite this article in press as: Merino et al., Nuclear proteome reveals microtubule-associated protein regulating fate and disease, Cell (2026), https://doi.org/10.1016/j.cell.2026.05.019

standard density of 10 localizations/μm^3 using the scaling relationship d_normalized = d_observed $\times$ (ρ_observed/ρ_standard)$^{1/3}$. Mean ratios and standard deviations were then calculated across all cells within each condition.

To assess subcellular MAP1B distribution, MAP1B densities between nuclear and somatic compartments for the control and MAP1B knockdown conditions were compared. Nuclear and somatic regions of interest (ROIs) were manually defined using Picasso software. For each ROI, the raw number of localizations was extracted, and the density of MAP1B per μm^3 calculated. The ratio of MAP1B in the nucleus to the soma was then determined.

Recombinant DNA

Recombinant DNA	Source	Identifier	IUE concentration*	Amount for transfection ^
Expression plasmid: pCAG-GFP-shControl	Dr. Adam O'Neill (gift)	shControl	700 ng/ul, 550 ng/ul#	1 ug
Expression plasmid: pCAG-GFP-shMap1b	This study	shMap1b	700 ng/ul, 550 ng/ul#	1 ug
Expression plasmid: pCAG-GFP-shMap1b#2	This study	shMap1b#2	700 ng/ul	1 ug
Expression plasmid: pDCX-GFP-shControl	This study	pDCX_shControl	1000 ng/ul	-
Expression plasmid: pDCX-GFP-shMap1b	This study	pDCX_shMap1b	1000 ng/ul	-
Expression plasmid: pCAG-ires-RFP	This study	RFP	590 ng/ul	1,08 ug
Expression plasmid: pCAG-NESMap1b-ires-RFP	This study	NES-Map1b	1294 ng/ul	2,36 ug
Expression plasmid: pCAG-NLSMap1b-ires-RFP	This study	NLS-Map1b	1300 ng/ul	2,37 ug
Expression plasmid: pCAG-3xFlag-Map1b-ires-RFP	This study	MAP1B 1-2465	-	1 ug
Expression plasmid: pCAG-3xFlag-Map1b(1-848)-ires-RFP	This study	MAP1B 1-848	-	0,6 ug
Expression plasmid: pCAG-3xFlag-Map1b(524-848)-ires-RFP	This study	MAP1B 524-848	-	0.5 ug
Expression plasmid: pCAG-3xFlag-Map1b(1-523)-ires-RFP	This study	MAP1B 1-523	-	0,6 ug

*Per embryo; ^ per 12 mm coverslip; #when co-electroporated with other plasmids

shRNA sequences

Name	Binding region	ssOligonucleotide sequences
shControl	-	Top: AAATGTACTGCGCGTGGAGACGTTTTGGCCA CTGACTGACGTCTCCACGCAGTACATTT Bottom: AAATGTACTGCGTGGAGACGTCAGTCA GTGGCCAAAACGTCTCCACGCGCAGTACATTT
shMap1b	*Map1b* 3' UTR	Top: TGTACATTCAAGTCACTTCCTGTTTTGGCCA CTGACTGACAGGAAGTGTTGAATGTACA Bottom: TGTACATTCAACACTTCCTGTCAGTCAGTG GCCAAAACAGGAAGTGACTTGAATGTACA
shMap1b#2	*Map1b* ORF	Top: ATCAAACGCACCTCAGTGCTGGTTTTGG CCACTGACTGACCAGCACTGGTGCGTTTGAT Bottom: ATCAAACGCACCAGTGCTGGTCAGTCAGTGG CCAAAACCAGCACTGAGGTGCGTTTGAT

Please cite this article in press as: Merino et al., Nuclear proteome reveals microtubule-associated protein regulating fate and disease, Cell (2026), https://doi.org/10.1016/j.cell.2026.05.019

Docking site sequences

Handle name	Sequence	5'-mod	3-mod	Vendor
R1	TCCTCCTCCTCCTCCTCCT	C-3 azide	None	Metabion
R3	CTCTCTCTCTCTCTCTCTC	C-3 azide	None	Metabion
R4	ACACACACACACACACACA	C-3 azide	None	Metabion
R6	AACAACAACAACAACAACAA	C-3 azide	None	Metabion

Experimental parameters for DNA-PAINT imaging

Target No.	Target name	Species	1ry AB dilution	2ry NB dilution	Imager	Imager conc. (pM)	Incubation
1	BRG1	Rabbit	1:200	1:200	R1/R6	100/120	1^{ry} oN, 4 °C, 2^{ry} 1h, RT the next day
2	MAP1B	Mouse	1:200	1:300	R3	80-120	pre-incubation
3	ACTB	Mouse	1:200	1:200	R4	80-100	pre-incubation
4	PAX6	Mouse	1:300	1:300	anti-mouse IgG1 647	-	1^{ry} oN, 4 °C, 2^{ry} 1h, RT the next day

Experiments were carried out in buffer C+ containing 1x PCD, 1x PCA and 1x Trolox, prepared freshly for each imaging round.

QUANTIFICATION AND STATISTICAL ANALYSIS

MAP1B knock-down efficiency in E14 cultures was assessed by quantifying the mean intensity of MAP1B immunostaining per transfected neuron after averaging intensity Z projection. Each n corresponds to a transfected neuron, being n=60 for shControl and shMap1b, and n=38 for shMap1b#2 condition, coming from three and two independent cultures, respectively. Effects were tested using Kruskal-Wallis test followed by Dunn's multiple comparison testing.

For tissue organization analysis of *in utero* electroporated brains, two to three coronal sections from three to eleven embryonic brains coming from at least two litters for each treatment were analyzed. For quantifying the distribution of electroporated cells, the position of the GFP+ cells was assessed by counting the number of GFP+ cells in a 5-binned cortex divided by the total amount of GFP+ in the cortical column analyzed. Effects were tested by performing two-way ANOVA followed by Dunnett's or Šídák's multiple comparisons test.

For live imaging analysis of organotypic slices, cells derived from four electroporated brains originating from two different mothers were analyzed, consisting of a total number of 146 cells coming half from the shRNA control condition and half for shRNA Map1b condition. In each imaging session, organotypic slices of electroporations from both conditions were imaged together. Cell movements were quantified using the FIJI plugin MTrackJ after performing a maximum intensity projection for each timeframe. Cell's speed was quantified by dividing the distance travelled (μm) per hour and tortuosity was assessed by dividing the distance travelled (μm) by the cell's net displacement. For subpopulation analysis, a series of Gaussian mixture models with an increasing number of components was fitted to the log-transformed resulting data, and a best fitting solution of three clusters was obtained by minimizing the Bayesian Information Criterion. The treatment distribution per cluster was tested against the null hypothesis of balanced proportions using Fisher exact test.

For live imaging analysis of E12 cortical cultures, GFP+ cells present in five to six field of view for each well were followed for 24 hours using FIJI, starting 6 hours after the beginning of the recording to allow cells to stabilize to the microscope set up. Only cells that could be followed over all times were tracked, and cells categorized as deriving from the meninges based on cellular morphology were omitted for the analysis. Both cell death and the number of cells present in each time point were assessed with the help of the brightfield channel. For assessing the percentage of cell survival, the total number of cells present at the endpoint of analysis was divided by the total maximum number of cells that would be present if no cell death had occurred. Percentage of cell survival was tested by using Wilcoxon test.

Cell identity after electroporation or transfection was assessed using FIJI and analyzed by dividing the number of GFP+ Marker+/- or GFP+ Marker+/- cells by the total number of GFP+ or GFP+ RFP+ cells counted per biological replicate (cortical culture or embryonic brain). Effects were tested by performing two-way ANOVA followed by Šídák's multiple comparisons test when assessing cell identity using two markers, Mann-Whitney/Kruskal-Wallis test followed by Dunn's multiple comparison testing when using one marker or paired one-way ANOVA + Geisser-Greenhouse correction followed by Dunnett's multiple comparisons testing when treatments were performed in common initial cortical cultures.

Please cite this article in press as: Merino et al., Nuclear proteome reveals microtubule-associated protein regulating fate and disease, Cell (2026), https://doi.org/10.1016/j.cell.2026.05.019

For studying MAP1B/Flag/MYC staining levels in the nucleus and soma, confocal images from cell cultures or brains were obtained using Z steps of 0.05-1 μm. The mean intensity in both compartments for each cell was measured in the Z stack at the center of the nucleus. Effects were tested by performing two-way ANOVA followed by Šídák's multiple comparisons test when assessing levels in both nucleus and soma or two-tailed Mann-Whitney test (=2 conditions) or Kruskal-Wallis test followed by Dunn's multiple comparison testing (>2 conditions) for comparing MAP1B's nuclear/soma intensity ratio. Outliers were identified and removed if significantly tested by the ROUT method (Q=1).

To study the presence of ectopic neurons in the ventricular zones from cerebral organoids, three independent batches of cerebral organoids were generated, and around 8-9 PAX6+ cortical-like structures per batch and per line were selected and imaged in a confocal microscope for further analysis. VZs without any MAP2+ cell were categorized as "*Clear*", whereas the VZs positive for MAP2 staining (including processes and/or cell bodies) were categorized under MAP2+. Effects were tested by two-way ANOVA matched (paired per batch), followed by Fisher's least significant difference test.

To study the thickness of the PAX6$^+$ and MAP2$^+$ regions and their ratio, three independent batches of cerebral organoids were analyzed. Cortical-like structures with clearly defined MAP2$^+$ boundaries were selected for further analysis. This resulted in 2–6 cortical-like structures per batch and line, with a total of N = 11 for WT organoids and N = 14 for MAP1B KI organoids. For each cortical-like structure, three random thickness measurements were obtained and averaged to generate a single mean thickness value per structure. These averaged values were used to compare PAX6$^+$ and MAP2$^+$ region thicknesses between genotypes. The PAX6$^+$/MAP2$^+$ ratio was calculated by dividing the averaged PAX6$^+$ thickness by the averaged MAP2$^+$ thickness for each cortical-like structure. Statistical differences between genotypes were assessed using a two-tailed unpaired *t*-test, following confirmation of normal data distribution using the Shapiro–Wilk, D'Agostino & Pearson, Anderson–Darling, and Kolmogorov–Smirnov tests. Outliers were identified and excluded using the ROUT method (Q = 1).